A STUDY OF THE MORPHOLOGY OF POROSITY IN SINTERED URANIUM-ZIRCONIUM ALLOYS AS A FUNCTION OF SINTERING TIME

A Thesis

by

CLIFFORD SHANE HART

Submitted to the Office of Graduate and Professional Studies of
Texas A&M University
in partial fulfillment of the requirements for the degree of

MASTER OF SCIENCE

Chair of Committee,	Sean M. McDeavitt
Committee Members,	Lin Shao
	Patrick Shamberger
Head of Department,	Yassin Hassan

May 2019

Major Subject: Nuclear Engineering

ABSTRACT

Uranium- 10 wt. % zirconium (U-10Zr) alloys were generated using powder metallurgy methods to create porous specimens with densities ranging from 70 to 98 % Theoretical Density (%T.D.). This was completed as part of a larger project funded by the U.S. Department of Energy designed to use computational and experimental methods to evaluate the sintering behavior in U-10Zr metallic fuel for advanced nuclear fuel simulations in the MOOSE/MARMOT simulation environment.

Uranium microspheres (180 to 45 micron in diameter) produced in the Rotating Electrode System (RES) were mixed with purchased zirconium microspheres (<44 micron diameter). This powder was thoroughly mixed and pressed in a six millimeter die at 8,000 pounds force to form the green pellets. Subsequently, the pellets were measured, weighted, density calculated, and sintered at varying times from two to twelve hours. The resultant pellet was then re-measured for density, cut in a fashion that exposed the radial and axial center-line faces, polished, imaged in a Scanning Electron Microscope (SEM), and the image analyzed for porosity area fractions and morphology.

As expected, longer sintering times result in more dense samples. However, due to deformation of the exterior of the pellet during pressing and sintering, alloying density changes, spring back, and pore migration, the change in density was far from linear. Additionally, pore sizes increased before finally decreasing as they migrated to uranium sphere boundaries. Pores converged into softer zirconium channels near the uranium sphere boundaries before dispersing as sintering time increased.

DEDICATION

I dedicate this work to the people who have supported me the most in this endeavor: to my wife and children, Tracie, Alicia, and Janie, thank you.

ACKNOWLEDGMENTS

I would like to thank God, without whom I would have never had the strength to make it here. A great debt of gratitude also to my mentor and committee chair, Dr. Sean McDeavitt who has managed to support and encourage me with seemingly endless patience despite his immensely busy schedule. I would like to thank my committee chairs, Dr. Shao and Dr. Shamberger, for their support and guidance. Additionally, I extend a special thank you to Nuclear Engineering Department Head Dr. Hassan for his support in my time of need.

Thanks also goes to my friends and colleagues: To Dr. Ortega and Dr. Perez-Nunez who supported my research every step of the way while managing the lab and keeping me safe. Thanks to Jordan Evans who listened and critiqued my theories, ideas, and methodologies. Thanks to Yesenia Salazar who worked this project with copper and helped with equipment and ideas. Finally, thanks to my wife and children for their encouragement, space when I needed to study or write, and an endless supply of caffeine when I needed it.

NOMENCLATURE

BCC	Body Centered Cubic
DU	Depleted Uranium
EDS	Energy Dispersion Spectroscopy
HCP	Hexagonal Close Packed
NU	Natural Uranium
RES	Rotating Electrode System
PPE	Personal Protection Equipment
PPM	Parts Per Million
SEM	Scanning Electron Microscope
TAMU	Texas A&M University
TIG	Tungsten Inert Gas
U10Zr	90% by weight Uranium with 10% by weight Zirconium
VFD	Variable Frequency Drive

TABLE OF CONTENTS

LIST OF FIGURES

Page

Page

Page

LIST OF TABLES

1. INTRODUCTION

Uranium- 10 wt. % zirconium (U-10Zr) alloys were generated using powder metallurgy methods to create porous specimens with densities ranging from 70 to 98 % Theoretical Density (%T.D.). This was completed as part of a larger project funded by the U.S. Department of Energy designed to use computational and experimental methods to evaluate the sintering behavior in U-10Zr metallic fuel for advanced nuclear fuel simulations in the MOOSE/MARMOT simulation environment [1, 2].

Team members at the University of Arkansas performed a parametric simulation study focused on the relationship between sintering rate and the distribution of pore size [3, 4, 5]. Team members at Georgia Tech worked to atomistically simulate metallic uranium interfacial properties relevant to sintering [4, 6]. As a companion to the data reported in this document, a study was completed by Salazar at Texas A&M University [7] using copper metal; the single-component sintering images are desirable for benchmarking the phase field and atomistic models noted above.

This study was undertaken to generate characterized, controlled porosity distributions in sintered U-10Zr samples with documented process variables and microstructure images to facilitate future sintering simulations and model validation. To this end, U-10Zr samples were fabricated by mixing uranium metal microspheres with zirconium powder. The powder mixtures were pressed in a 6 mm stainless steel die with a pressure of 5.93 MPa. The green pellets had a nominal density between 60 and 85 %T.D. and were sintered under flowing argon at temperatures ranging from 900°C to

1100°C resulting in final sample densities ranging from 68 to 86 %T.D. The sintered samples were carefully measured, sectioned, and polished for imaging.

The depleted uranium microspheres were manufactured using a rotating electrode system (RES) in the Fuel Cycle and Materials Laboratory at Texas A&M University. This system was built by Thompson [8] and installed inside an inert atmosphere glovebox by Galicki [9] and used for this work. The microspheres from the RES were sieved to provide particle sizes ranging from 45 to 180 μm. The zirconium metal powder was purchased (Materion, Clevland, Ohio) with a nominal particle size of ≤45 μm.

The green samples were sintered at temperatures above 863°C to guarantee that both metals exist with body-centered cubic crystal structures (β-Zr and γ-U). This common structure and the intimate surface contact after pressing facilitated diffusive alloying during sintering. Therefore, in addition to the final pore distributions desired for the model activities, the diffusive mixing of the powder was also examined by performing shortened sintering tests with subsequent metallography.

Therefore, this document contains the following information. Chapter 2 provides a review of uranium, zirconium, and U-10Zr properties along with discussions on diffusion and alloying, the RES equipment used to create DU microspheres, and metal sintering. Chapter 3 describes the equipment and procedures used to generate and characterize the porous U-10Zr samples. Chapter 4 compiles the results from this study along with specific sample data and images to completely describe each sample for future utilization. Chapter 5 surveys the data and discusses the overall meaning of the entire data set. Chapter 6 summarizes the data and describes future work in this area.

2. BACKGROUND

The Sections in this chapter present background information on relevant physical properties of uranium, zirconium, and U-10Zr alloys (Section 2.1), the rotating electrode system used to manufacture the uranium microspheres (Section 2.2), and the diffusion based alloying that occurs during sintering (Section 2.3).

2.1 Physical Properties of U, Zr, and U-10Zr

Table 2.1: Uranium and Zirconium Properties. Reprinted from [10]

	Phase Polymorphs	**Transition Temperatures**	**Density** *(at 25°C, 1 atm)*	**Yield Strength**
Uranium	α-U (orthorhombic) β-U (tetragonal) γ-U (BCC)	α→β 668°C β→γ 775°C γ→L 1,132°C	19.05 g/cm^3	380 to 625 MPa *(impurity effects)*
Zirconium	α-Zr (HCP) β-Zr (BCC)	α→β 863°C β→L 1,855°C	6.52 g/cm^3	330 MPa

Table 2.1 presents relevant properties of uranium and zirconium metal [10]. This data includes the basic crystal structure allotropes for both metals and their associated transition temperatures. It is commonly understood that metals with similar structures such as the BCC β-Zr and γ-U will be more likely to exhibit high mutual solubility, which will enable diffusive alloying during sintering. The density values are needed to enable estimating the density of powder mixtures. The yield strength is relevant when

considering the pelletization pressures required for sample preparation.

Solubility can be better understood as a measure of atomic mobility. A low solubility will limit the rate of relaxation, the release of residual stresses. A high solubility will result in faster and more complete mixing. The solubility of alloys with uranium in its different phases is shown in Figure 2-1 [reprinted from 11].

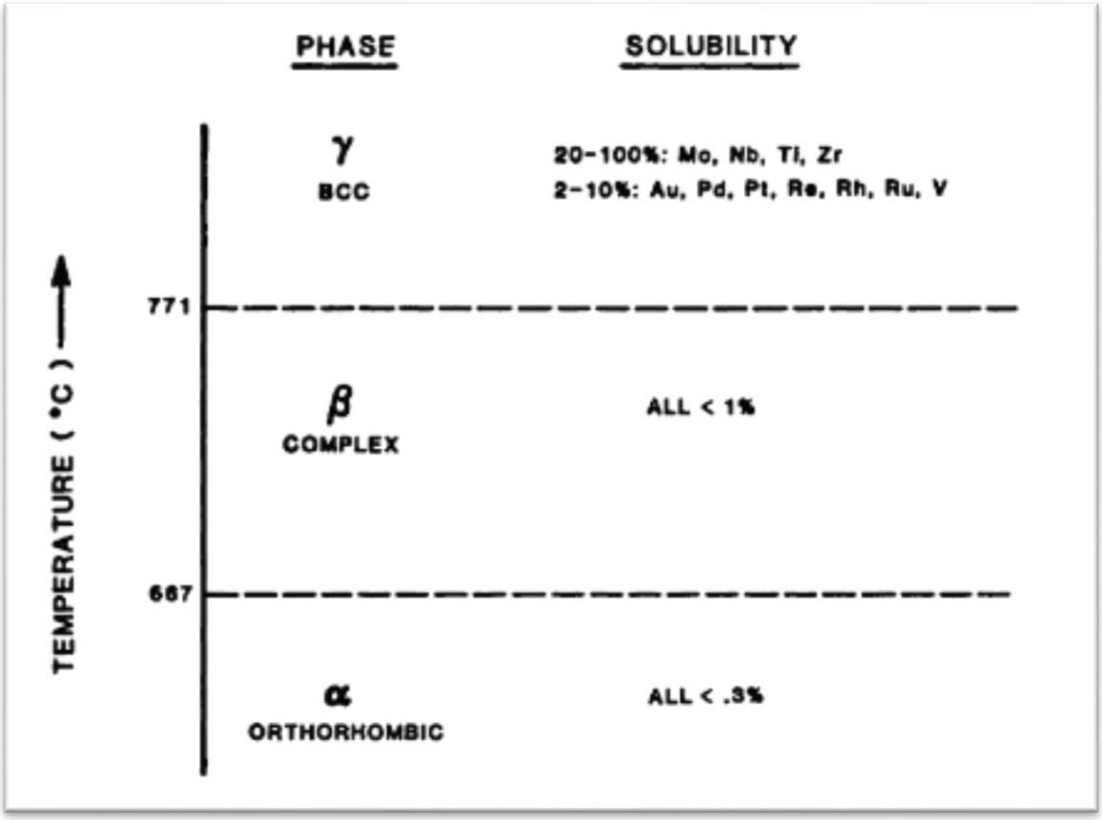

Figure 2-1: Polymorphism and solubilities of alloying elements in uranium. Reprinted from[11]

Stress Relaxation is a function of residual stress after pressing and can affect the pellet volume and therefore density. However, according to K.H. Eckelmeyer, the

amount of stress relaxation in uranium and its compounds after the first seconds of pressing, at temperatures below 200°C, is negligible [11]. This means that changes in volume due to relaxation are not a concern for green pellet measurements. This stress relaxation does however, become a concern during sintering. Figure 2-2 shows a representation of the effects of temperature and time on stress relaxation in annealed unalloyed uranium [reprinted from 11]. This is a concern because relaxation will cause volumetric expansion and this expansion will oppose densification. Additionally, this expansion will most likely not be uniform and will skew dimensional volume measurements.

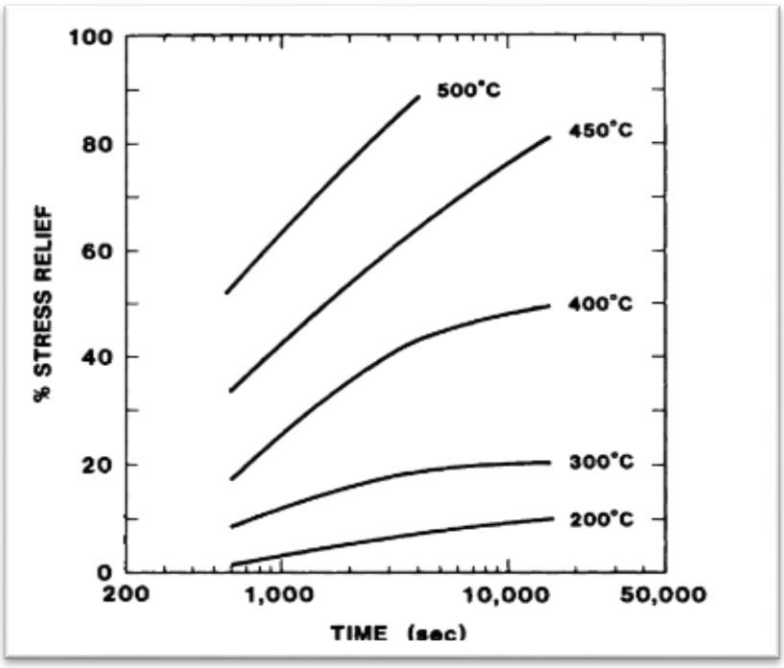

Figure 2-2: The effects of temperature and time on stress relaxation in annealed unalloyed uranium. Reprinted from [11]

The binary U-Zr diagram phase is shown in Figure 2-3 [12]. The transition temperatures for 10 wt% zirconium are 662°C for alpha to beta and 693°C for beta to gamma transformation according to Howlett and Knapton and is shown in Figure 2-3 [reprinted from 12]. Therefore, once uranium transforms to gamma phase, around 771°C, the solubility greatly increases and mixing is faster and more complete.

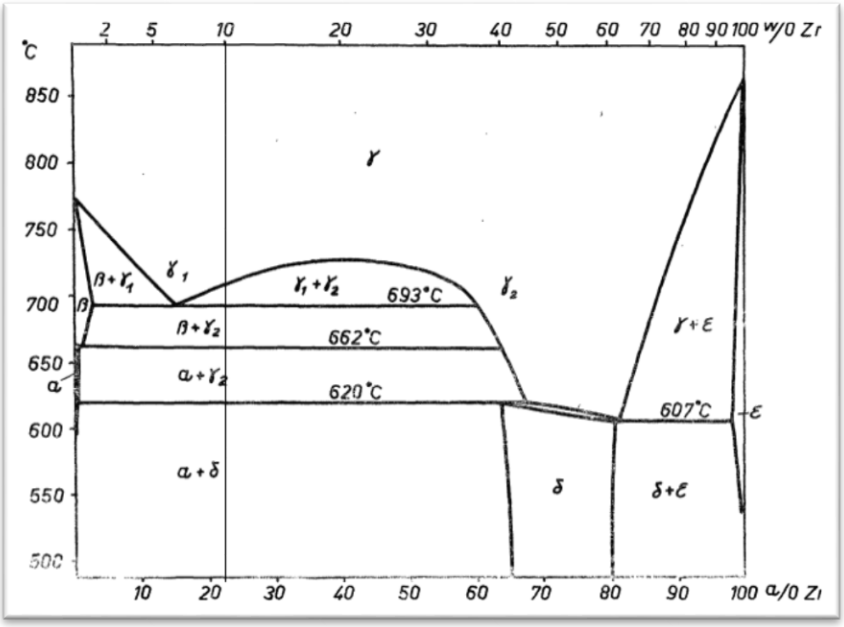

Figure 2-3: U-Zr phase diagram with line drawn at 10 wt% Zr. Reprinted from [12]

The diffusion of zirconium into uranium, and in the other direction, is of interest because of mixing that occurs during the sintering. Specifically, the penetration distance of this reaction is important. Penetration distance is defined as the depth into the original interface surface of two dissimilar materials in which mixing first occurs. Mash and Disselhorst used the diffusion equation, equation 2-1, and developed equations 2-2

to solve for the depth of diffusion for various times in gamma phase with uranium and zirconium. [13]

$$x = Kt^{0.5} \quad \text{2-1}$$

$$K = 3.36 \times 10^5 e^{\frac{-25800}{RT}} \quad \text{2-2}$$

where x is penetration depth in microns, K is a penetration coefficient in microns/hr$^{1/2}$, t is time in hours, 3.36 x 10^5 is the penetration coefficient constant solved by Mash and Disselhorst, 25,800 calories is the activation energy of diffusion for uranium and zirconium, R is the universal gas constant 1.987 cal/K-mol, and T is temperature in Kelvin. These equations can provide an idea of the completeness of mixing by estimating the penetration depth.

2.2 Rotating Electrode Systems for Metal Powder Production

The uranium powder used in this study was produced by the author using a previously established rotating electrode system (RES) [8, 9]. The process generates metal microspheres by arc-melting the tip of a rotting electrode in an inert atmosphere. The spheres are generated with particle sizes ranging from 44 to 510 micron.

The RES was built based on previously demonstrated designs; the original system was developed by the Starmet Corporation in 1972 [14] and a similar system was built at Idaho National Laboratory in 2007 [15]. A schematic representation of the Starmet RES is shown in Figure 2-4 [reprinted from 14]. The process is a centrifugal atomization method of metal powder production that is characterized by a relatively tight particle size distribution [16]. The system consists of three parts: a rotating spindle, an arc or

plasma welder, and a catch or containment system.

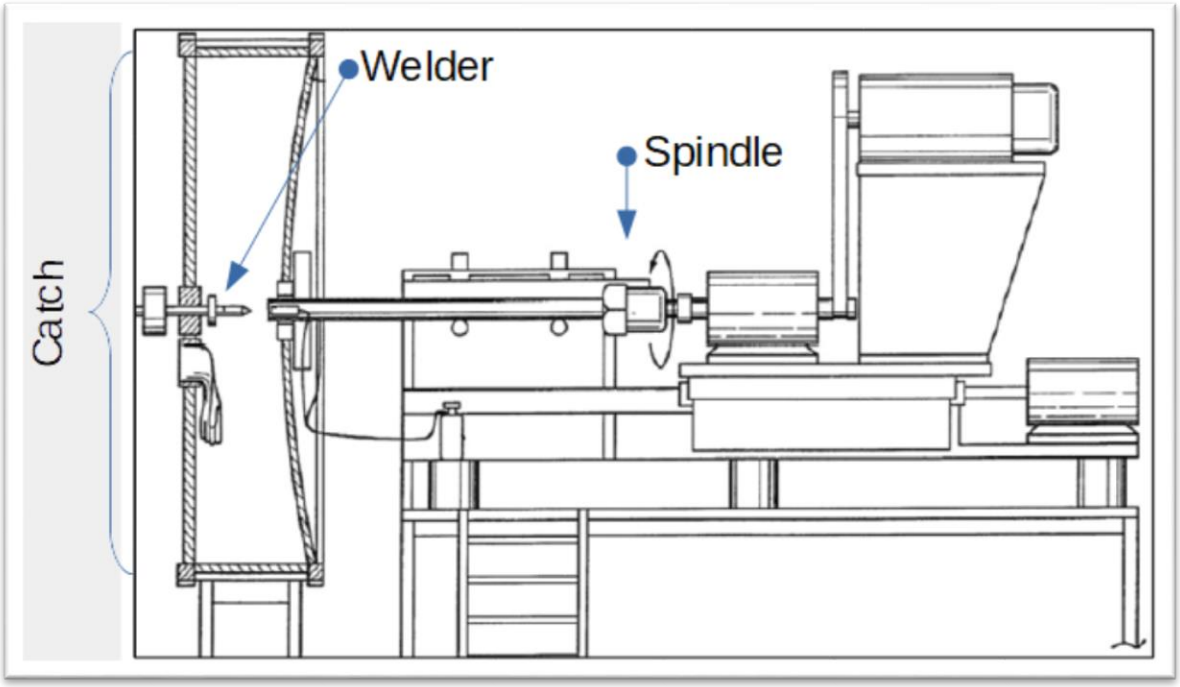

Figure 2-4: The Starmet Rotating Electrode System. Reprinted from [17]

The rotating spindle has two functions: it must securely hold and spin the metal rod and it must be able to pass current through the rod. The speed of the RES motor is controlled by a Variable Frequency Drive (VFD) controller. Securing the rod while spinning at high RPMs is very important. Once an arc is established and the metal begins to increase in temperature, it becomes more ductile and is susceptible to bending in response the intense forces associated with rotation. The system used for this work operated below 18,000 RPM but some systems, such as vertically mounted ones, rotate at speeds two to three times that speed [18].

The current passing through the arc welder tip must be adjusted to ensure that melting begins rapidly once the arc is established. Once this occurs, liquid metal powder is thrown outward in a radial spray as the centrifugal force overcomes the surface tension forces. The electrical current is passed into the welder tip utilizing carbon brushes attached to the spindle system via a slip ring. The RES slip ring and brush system is shown in Figure 2-5 [reprinted from 8]. Current flows through the carbon brushes into the metal shaft. The circuit continues from the shaft, past the non-motorized spindle, into the collet (not pictured). The collet holds the sample rod to be melted and completes the circuit through the sample.

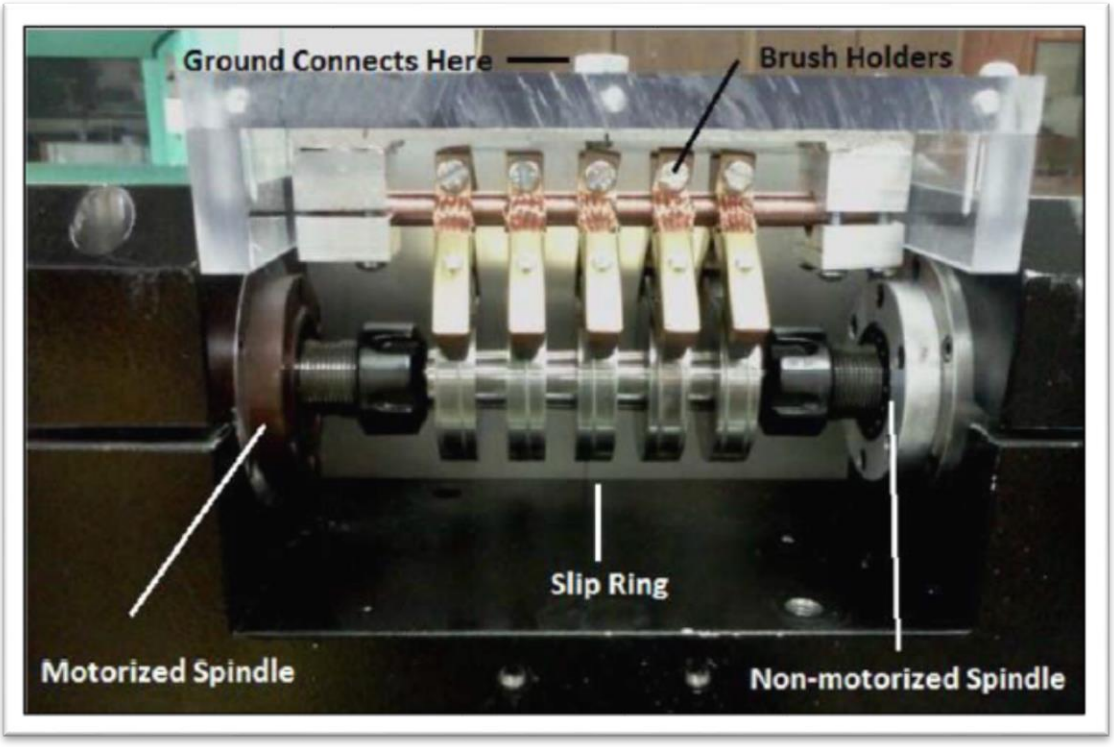

Figure 2-5: The RES slip ring mounted with the electro-graphitic brush system. Reprinted from[8]

The welder in the RES is a Lincoln Electric Precision TIG 225 arc welder. The welding probe is attached to the outside of the catch pan which was attached to a carriage system. This allows the probe to be moved closer to the rod as melting occurred in order to maintain the arc. Current passes from the welding power supply, through the welding tip (probe), to the rotating metal rod, into the spindle system, and to the slip rings. From the slip rings, the current is transmitted into graphite brushes in spring-loaded contact with the slip ring faces and current returns to the power supply to complete the circuit. A cover gas flow is directed at the tip of the welding probe that blows over the metal rod as melting occurs facilitating cleaning and cooling of the metal. Both ultra-high purity helium and argon have been used as cover gases but the higher thermal energy removal with helium produced undesirable powder distributions with uranium and so argon was used as the cover gas for this work.

A catch-pan assembly was used to collect the flying microspheres. This assembly is simply a shield placed around the rotating rod that catches solidified powder and diverts it into a collection system. The outer wall of the shield is far enough removed from the liquid drop ejection to ensure cooling and solidification occurs.

Ultra-high purity helium was injected into the catch pan using nozzles to direct the gas flow along the walls of the catch pan. This improved the convective heat transfer during cooling of the microspheres before hitting the catch pan wall. The collection system involved a tray at the bottom of the catch pan. After particles solidify and bounce off the shield, gravity, with some assistance from the helium cooling flow, forces them into the collection tray.

2.3 Sintering

Sintering is a process wherein a compressed powder or porous body densifies at an elevated temperature, usually without melting the material. In this study, the sintering of uranium-zirconium samples is accomplished which adds the additional phenomenon of diffusional mixing of the two components. For completeness, a brief review of sintering mechanisms is presented here.

Sintering is a diffusion driven process that reduces surface energy and relieves internal stresses. Sintering can occur in metallic, ceramic, and polymer systems to produce solid objects with designed shapes. Before sintering, the powder of interest is pressed into a low density "green" form that is typically between 5 and 70 %T.D. The green body is then heated to a temperature that increases the atomic mobility, promotes grain growth, promotes bonding, and thus enables sintering [18, 19]. The control variables for sintering include the pressing pressure, sintering temperature, and sintering time.

There are multiple mechanisms that enable sintering; plastic deformation, grain boundary diffusion, lattice diffusion, surface diffusion, and vapor transport. For metal sintering, the dominant densification mechanisms tend to be the first two listed and the third conditionally. Lattice diffusion from the grain boundary is important for densification when the atom diffusing comes from the grain boundary. However, if the atom comes from the surface, it is a non-densifying mechanism.

Consider that the compacted "green structure" can be represented by hundreds of

spheres packed tightly into a bucket. At the point where the spheres contact each other, a small amount of weak glue is applied. Once dried, this shape can be pulled out of the bucket and it will hold the shape of the bucket. However, there is a lot of empty space inside the shape no matter how many spheres of whichever size that was forced into the bucket. Also, the small contact-points represented by the glue are very weak and any force applied to the shape is likely to cause a break. Particularly, spheres at the edges of the top and bottom of the cylinder are the weakest because they have the fewest contact-points. Similarly, green bodies typically have densities much lower than theoretical density. The green body is very weak due to lack of bonds between particles and in no way compares to the strength of the bulk material [20].

As the green body is heated, typically to half the absolute melting temperature or higher, diffusion of particles between the spheres at these contact points begin. This causes the growth of "necks" between the particles. As these necks increase in size, the diffusion rate increases due to increased surface area for diffusion to occur. These necks also vastly improve the strength of the material and begin closing the voids within the shape. Eventually, and gradually, with enough sintering time, the material will approach close to the theoretical density and strength of the bulk material [21].

The large amount of surface area in the green body provides the main driving force for sintering: a reduction in surface energy. As necking occurs between microspheres, surface area is reduced and therefore surface energy is reduced. The mechanisms for this material transport can be summed up into two broad categories: surface transport and bulk transport [21, 22]. Surface transport involves mass moving around the particles

surface to the contact point thereby forming the neck. This form of transport doesn't involve shrinkage. Bulk transport involves mass from within the particles moving to the contact point and forming the neck. Bulk transport does involve shrinkage of the green body. Figure 2-6 demonstrates these two mechanisms and how shrinkage occurs.

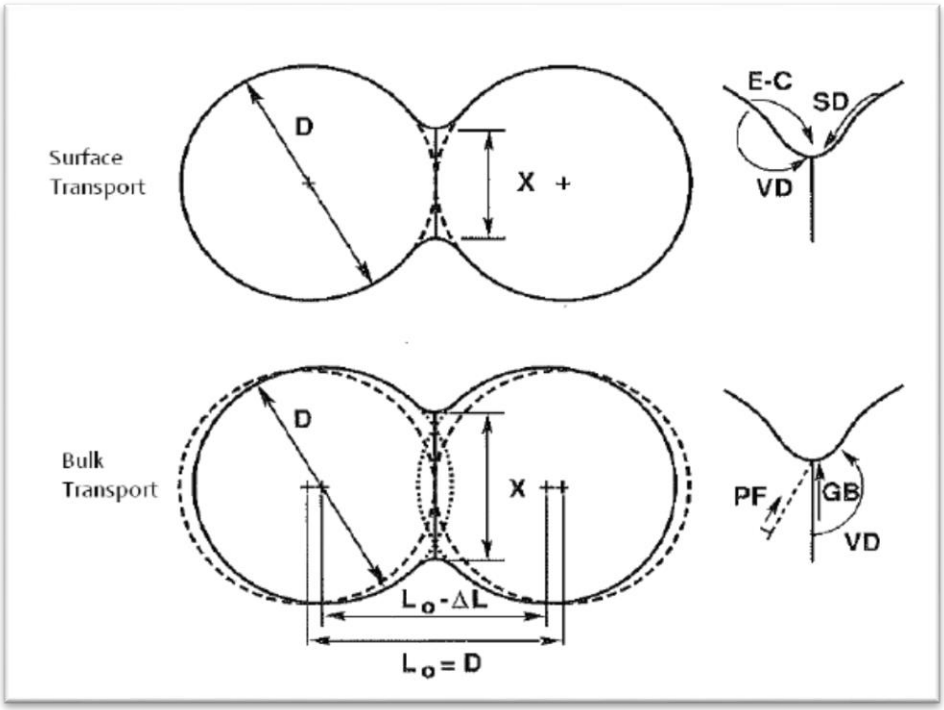

Figure 2-6: A visual representation of surface transport and bulk transport mechanisms, including evaporation-condensing (EC), surface diffusion (SD), volume diffusion (VD), grain boundary diffusion (GB), and plastic flow (PF) [21, 22]*

*Reprinted with permission from Sintering Theory and Practice by Randall M. German, 1996, Wiley, New York. Copyright [1996] by Wiley.

Evaporation-condensation occurs when surface atoms evaporate from a convex surface, transport through the void space, and condense onto a concave surface like the necking area. This mechanism does not change density of the material. This typically becomes a major contributor to necking at very high sintering temperatures near the melting point of the material and with a material that has a high vapor pressure [21, 22]. Surface diffusion involves the transport of atoms across the surface using surface defects. Surface diffusion doesn't require the high temperatures evaporation-condensation does and therefore is a contributor to most sintering processes [21, 22]. Again, there is no change in density with this mechanism.

Volume diffusion is driven by vacancy diffusion. Also referred to as lattice diffusion, volume diffusion does increase density. Vacancies are either filled during diffusion or migrate to the surface thereby densifying the microsphere. Grain boundary diffusion occurs when mass is transferred via grain boundaries to the growing neck region. As mass from internal grain boundaries migrate to this region, the neck region expands forming its own grains. Since this also involves mass transport from the center of the sphere to the contact-point, densification occurs. Finally, the plastic flow mechanism involves dislocation motion. Because this process consumes dislocations, it is limited to initial heating and under an applied stress, such as pressing [20, 22].

Volume diffusion is driven by vacancy diffusion. Also referred to as lattice diffusion, volume diffusion does increase density. Vacancies are either filled during diffusion or migrate to the surface thereby densifying the microsphere. Grain boundary diffusion occurs when mass is transferred via grain boundaries to the growing neck region. As

mass from internal grain boundaries migrate to this region, the neck region expands forming its own grains. Since this also involves mass transport from the center of the sphere to the contact-point, densification occurs. Finally, the plastic flow mechanism involves dislocation motion. Because this process consumes dislocations, it is limited to initial heating and under an applied stress, such as pressing [20, 22].

Topographical analysis of sintered bodies has been the subject of research for quite some time. Petru [23] pioneered studying particle size morphology of sintering just before Coble [24] took it up in the U.S. Coble studied the micro-stresses that affect the efficiency of sintering in a bimodal system. Both researchers inspired the model style analysis described above, however the method used in this study was completely different since it accounts for alloying and since the two elements have extremely different compression behavior.

3. EXPERIMENTS

This chapter describes the equipment utilized and the procedures followed for powder production, pellet production, polishing, and analysis. The following sections describe equipment and procedures for the production of uranium powder in the RES (Section 3.1), U-10Zr pellet pressing (Section 3.2), sintering (Section 3.3), post-sintering metallography and microscopy (Section 3.4), and image analysis (Section 3.5).

3.1 *Production of Uranium Microspheres Using the Rotating Electrode System, Sieves, and Mixing*

As noted in Section 2.2, the RES was used to produce uranium metal microspheres for the sintering experiments in this study. For the first three samples, Depleted Uranium (DU) rods were selected from existing stock in the lab. These rods were sanded with 400 grit sand paper as the only prep method. However, after testing showed that oxygen levels in these rods were above 20 atom%, a batch of Natural Uranium (NU) rods were used that were 99.9% NU with only surface oxidation. In order to minimize oxygen contamination, these rods were placed into a 50% by volume nitric acid bath for five minutes, rinsed with DI water, and then with ethanol before placing under a vacuum and transferring into the glove box. In the glove box, the rods were sanded and then wiped clean prior to use. Figure 3-1 shows the natural uranium rods in the nitric bath.

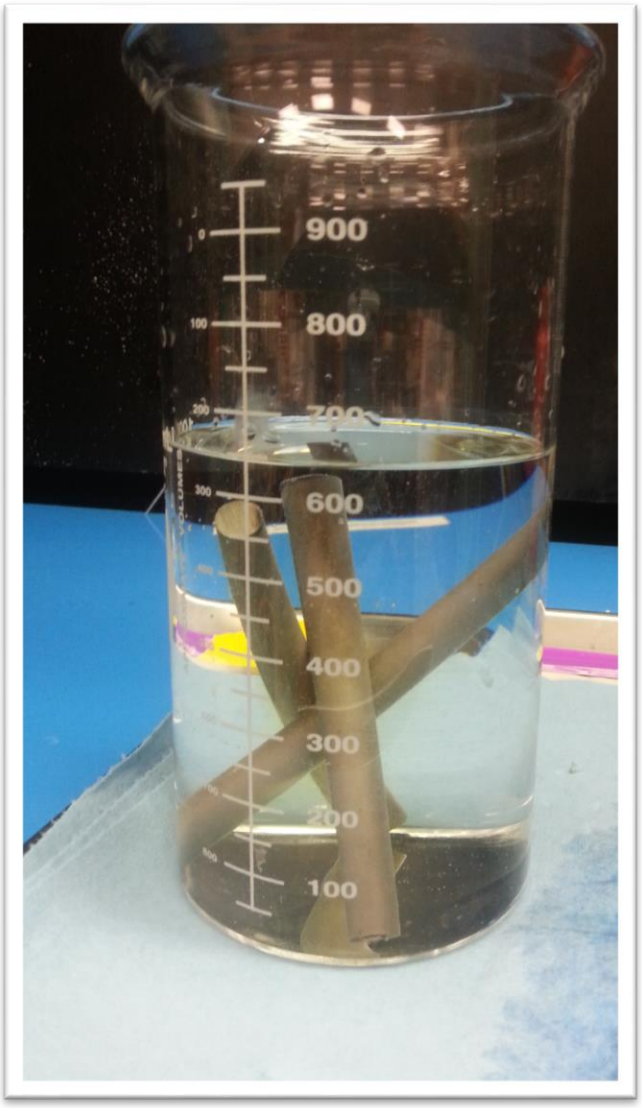

Figure 3-1: NU rods in a nitric acid bath

The RES produced uranium microspheres by spinning a 130 to 175 mm long, 10 mm diameter uranium rod at 15,000 to 19,000 rotations per minute (RPM) and melting the rod by discharging a Tungsten Inert Gas (TIG) welder current through the tip of the rod via the welder probe. The molten metal is ejected radially from the rod tip and cooled

by ambient argon gas before being collected in a catch pan. While traveling through the argon gas, surface tension reforms the molten metal into a sphere and then solidifies. The RES was designed by Thompson as a benchtop configuration with operation in air, as shown in Figure 3-2 [reprinted from 8]. The system was modified by Galicki to enable operation in an inert atmosphere glove box purchased from MBraun as shown in Figure 3-3 [reprinted from 9].

Figure 3-2: The RES original bench top configuration by Chad Thompson. Reprinted from[8]

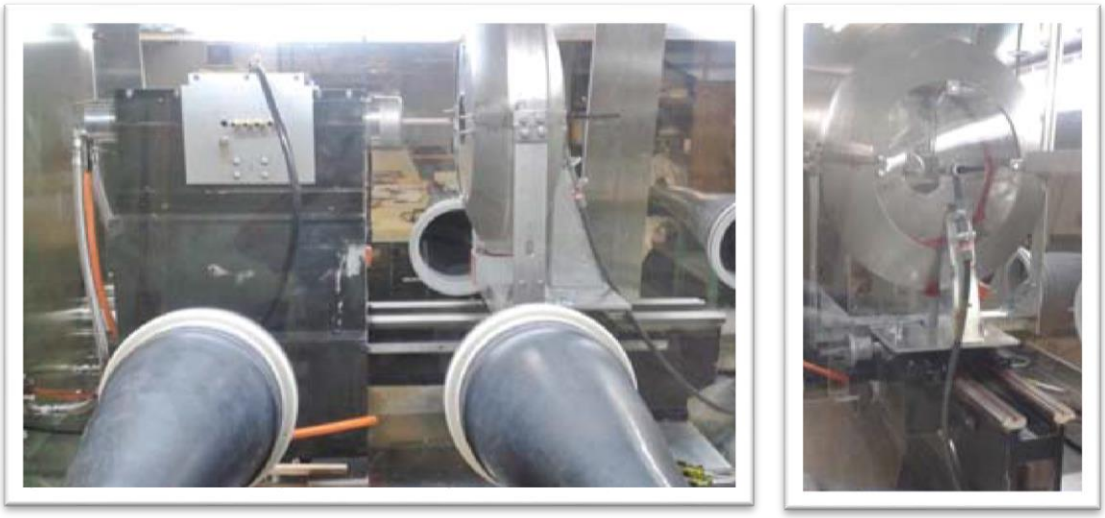

Figure 3-3: The refitted Rotating Electrode System by Galicki inside argon atmosphere glove box. Reprinted from [9]

The procedure used to generate the uranium microspheres was:

1. Prepare Metal Pins- Ensure the metal pin meets the size requirements for the collet used (5/8 to 1/2"). Insert the pin into the associated collet for its diameter. The pin should fit snuggly and not require hard tapping to insert (**DO NOT FORCE THE PIN BY HAMMERING IT IN**-it will damage the collet). Insert the pin approximately 1" into the collet.

2. Prepare the Catch Pan- If the pin being run is of a different material from the previous run, or characterization is sensitive for the run, remove the catch pan using the RES lift system and dismount the catch pan. Remove the Plexiglas cover and use the brush, scraper, and any other necessary tools to clean out the catch pan. After the pan is cleaned, remove the catch tray, carefully clean it out, and remove any remaining

particles from the catch tray area of the catch pan. Reinsert the catch tray and remount the catch pan on the RES carriage.

3. Water Flow and Spindle Fan- Ensure the chill water inlet and outlet valves are open (These are located behind the research furnaces and labeled RES). Plug in spindle cooling fan inside glove box, if unplugged.

4. Purge Air Lines- Ensure that the cooling air and cover gas tanks have pressure and that the tank valves are in the open position. For the cooling gas line, ensure the valve on the wall above the tank has been open. Back the welding probe away from the RES spindle by backing the catch pan carriage as far away as possible while staying on the tracks. Ensure the welder pedal is up and nothing is obstructing it. Plug in the TIG welder and turn it on. On the welder controls, lower the welder current to the minimum 5 Amps and increase post flow to 30 seconds. Tap the foot pedal until you see the flow meter register flow. Increase flow on the regulator until it is over 20 SCFM on the flow meter next to the motor controller. After the flow meter shows that flow stopped, press the foot pedal again. Repeat this until the flow requirement for the purge is met according to a) or b) below (30 sec/rep). During the final purge rep, adjust the cover flow using the regulator based on the reading on the flow meter near the motor controller and Equation 1 in this step. After flow has completed, ensure the foot pedal is up and increase the current on the welder to the desired experiment current. Decrease post flow to the minimum or whatever setting is desired. Turn off and unplug the welder.

In order to purge the cooling air, set the regulator to the desired flow according to Equation 2 below and open the purge valve above the cooling air line tap above the

glove box for the time necessary according to the purge guidelines below.

CFM Argon= SCFM Air x 0.852 (1)

CFM Helium=CFM Argon x 2.29 (2)

a) If tanks have pressure and the associated valves checked above were open, perform a standard purge of 3 mins (6 reps) or until glove box oxygen begins to drop on the cover gas line and 5 to 10 seconds on the cooling air line.
b) If a tank was empty or the isolation valves mentioned above were closed, perform an extended purge of 5 mins (10 reps) or until glove box oxygen begins to drop on the cover gas line and 10 to 15 seconds on the cooling air line.

Ensure glove box oxygen levels are lowered after the purge before continuing. This can be expedited by opening the cooling air isolation valve above the glovebox and purging UHP Helium into the box.

5. Prepare The Glove Box- Open the glove box pressure settings on the glove box controller. Note the current settings as you will return the system to these settings after the RES run. Lower the minimum pressure to 0.5 bar and the maximum to 3.0 bar. Set the upper hysteresis to 2.0 and the lower to 0.5. This will lower the glovebox pressure to 1 bar and will initiate venting early on in RES operation to prevent over pressurization of the glovebox.

6. Variable Frequency Drive Mode- Flip the breaker for the RES located across from the motor controller on the wall. Remove the protective front panel of the Variable Frequency Drive (VFD) electronics box and turn on the Variable Frequency Drive by flipping the breaker inside to the "up" position. It is designed to take two tries before remaining in the up position of its own accord but if the breaker was already up when the wall breaker was flipped, it will only take one lift. ***Replace the protective front panel***.

7. Welder Arrangement- Arrange the welder and foot troll pedal in a comfortable position for welding. Do not plug in the welder yet. Leave the front panel switch in the OFF position.

8. Pin Preparation- Insert your prepared metal pin and collet into the non-motorized spindle. Tighten the collet using your hand while using a wrench to hold the spindle from turning (This is a 2 person job for most people in the glovebox). Move the catch pan forward until the face of the metal pin is ~1/8" from the tip of the welding electrode and centered.

9. Welder Preparation- Ensure the foot troll pedal is fully "up" and clear of anything that might compress it (pressing the pedal down initiates current). The pedal should be on the ground next to the RES location and plugged into the welder. Plug the welder to a power source. Flip the front panel switch to the ON position. Ensure the welder is set to "DC Negative". Future experiments may require the welder to be set to AC or to different polarities of DC.

10. Initiate REP- Wearing appropriate personal protection equipment (PPE), set the VFD to spin the motor at around 5800 RPM by setting the keypad on the motor controller to 100. Rotations per minute can be calculated using Equation 3. Press the green start button.

RPM = (VFD Display #)*(38,900/667) (3)

Press the green button to initiate spinning. Keep your hand on the red button. When you see that the pin is spinning with no problems and minimum vibration, increase the RES

speed until the desired speed is reached. If vibration is too excessive during ramp up, press the red button to shut down. If necessary, push the metal pin farther into the collet to increase stability and return to the beginning of this step. After reaching the desired RPM, initiate cooling air flow by opening the isolation valve above the glove box and flip down welding helmet. When ready, press the foot troll pedal down until the arc is initiated. Continue pressing the pedal down until the tip of the pin begins to melt (should be fully pressed down if max current was properly adjusted on the welder). As the pin tip melts, maintain the 1/8" distance between the pin and the electrode by using the crank on the carriage to move the catch pan closer to the spindle. ***DO NOT allow the electrode to touch the rotating pin***, this will cause a short circuit. If only the inside of the pin melts, leaving a hollow shell, back off to allow the electric arc to cover and melt the shell. Continue until the catch pan comes into contact with the spindle holder and you can proceed no further. Release the pedal. Press the red button on the remote keypad. Shut the cooling air isolation valve. Return the glove box pressure settings to the original values (typical: lower-1 bar, higher-5 bar, both hysteresis-0.5 bar).

11. Ramp Down- Ensure the pedal is not depressed while ramping down the RPM (move aside with foot). The VFD mode should allow for minimum RPM while the brushes and slip ring cool off. Ensure enough time is allowed for proper cooling (~5 minutes). Turn off the VFD by flipping the breaker on the wall to the down position. Turn off the welder by flipping the front panel switch to the OFF position and unplugging the welder from its power source. Leave spindle cooling fan plugged in. Wait until pin is cool then remove from the collet. The powder will be in the powder

catch drawer at the bottom of the catch pan as shown in Figure 3-4.

12. Powder Sieving- Select the desired sieve ranges for characterizing or collection. Stack them in descending sizes with the largest on top. Place the sieves over an empty tray and funnel the powder into the top sieve. Place the lid on the top sieve and gently shake the stack while holding the sieves together tightly. Gentle tapping on the sides while slightly rotating the stack will increase the sieving speed and efficiency. After approximately 5 minutes of shaking, remove the top sieve and collect the powder inside. Repeat until each sieve is collected. The sieve stack is shown in Figure 3-5.

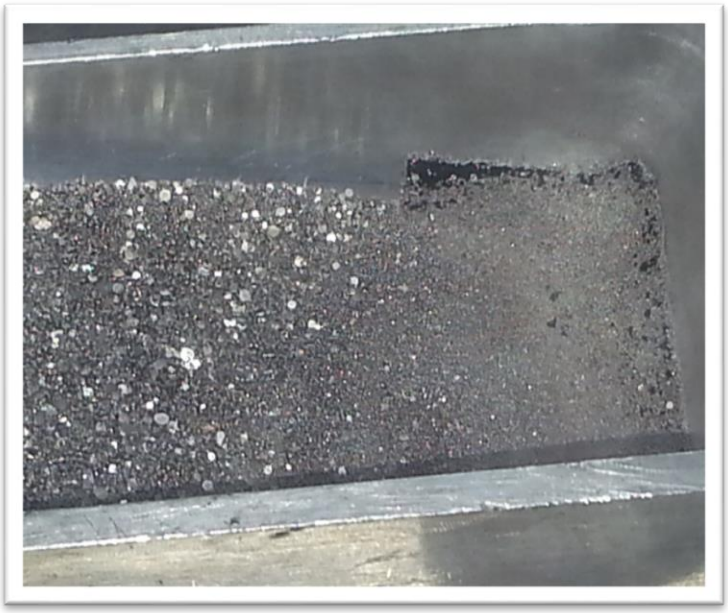

Figure 3-4: Uranium powder in the catch tray

Figure 3-5: Sieving stack with two sieve stages

For the purpose of this experiment, powders in the range of 45 to 180 micron were separated but not characterized in detail. A sample of these spheres, under an optical microscope, is captured in Figure 3-6. This powder was then mixed in bulk with a <44 micron zirconium powder to produce a 10 wt% zirconium mixture.

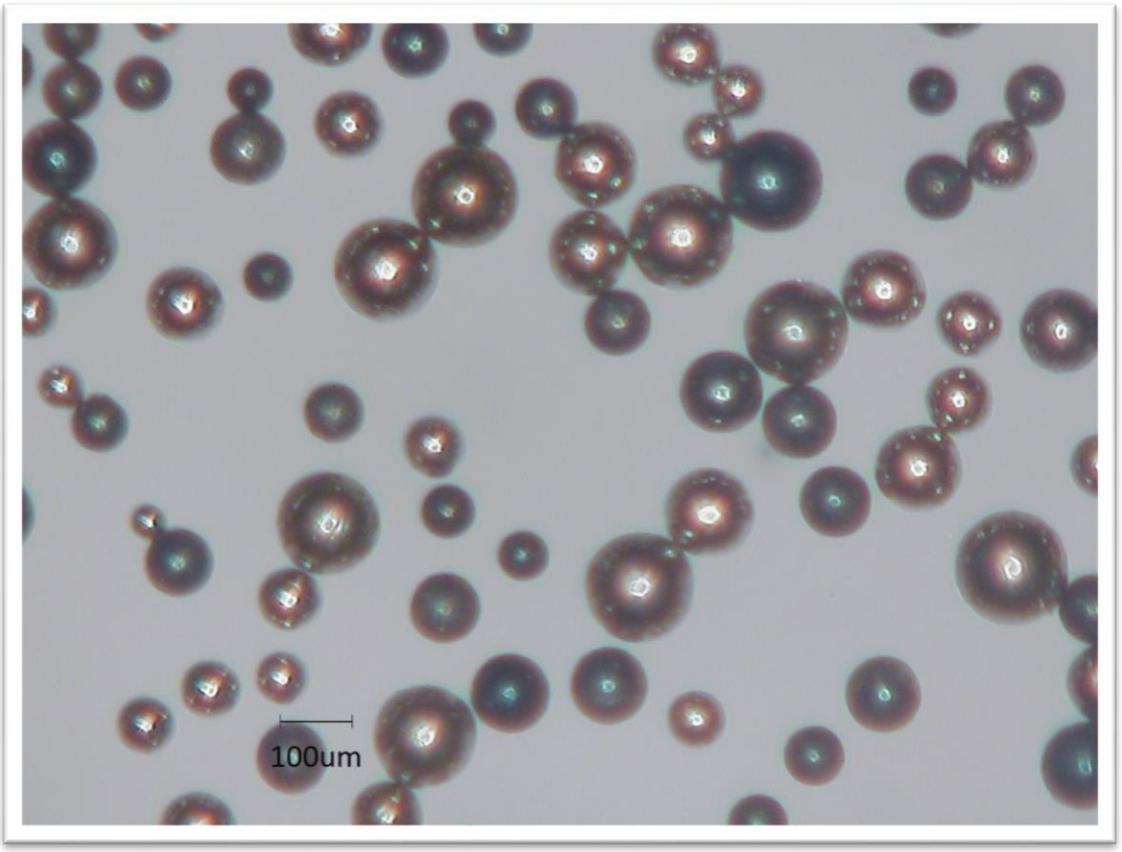

Figure 3-6: Uranium powder in the 45 to 180 micron range

3.2 Pellet Pressing

Depleted Uranium (DU) and Natural Uranium (NU) microspheres were produced using the procedures in Section 3.1. This U powder was combined with zirconium metal powder to produce a mass ratio of 10% zirconium and 90% uranium (U10Zr). Zirconium powder was purchased (Materion, Cleveland, Ohio) with a maximum 44 micrometer (-325 mesh) particle size. As noted above, the RES-derived uranium powder was sieved to use only the microspheres with diameters between 45 and 180 µm. To ensure adequate mixing, the powders were mixed in a large container and then placed on

rollers for 24 hours (i.e., the powders were mixed in a ball mill setup, but without the milling media).

A hydraulic Carver Laboratory Press Model C (Figure 3-7) was used inside an inert atmosphere glovebox to press the powder. A 6 mm diameter split die from Across International (model SDS6.K) used to press is also shown in the photo fully assembled on the pressing plate. Before pressing, the mass of the powder components is measured to create a U-10Zr mixture. After assembling the trapezoidal split inner sleeves on the base of the die, the outer sleeve slides over and secures and tightens the inner sleeves. At this point a push rod is used to ensure the trapezoidal sleeves are flat so that the splits between the seals are fully closed and the pellet will not be distorted. One of the die cores is lubricated with stearate and inserted into the chamber of the die with the push rod. A funnel is then used to pour the powder into the die with care taken to ensure all powder is used with negligible remnants.. The final die core is lubricated and pushed into the die with the push rod. The die is then inserted in the press and the pelletization pressure of 1260 MPa is applied for 60 seconds.

Figure 3-7: Hydraulic Carver press inside the glove box

Pellet pressing required some trial and error until the functional pressing protocol was established. In early pellets, there was delamination when the sample would press on one side but fall apart on the other. Other pellets would fail by sticking to the walls of the split die used which split the pellet into irregular pieces as shown in Figure 3-8.

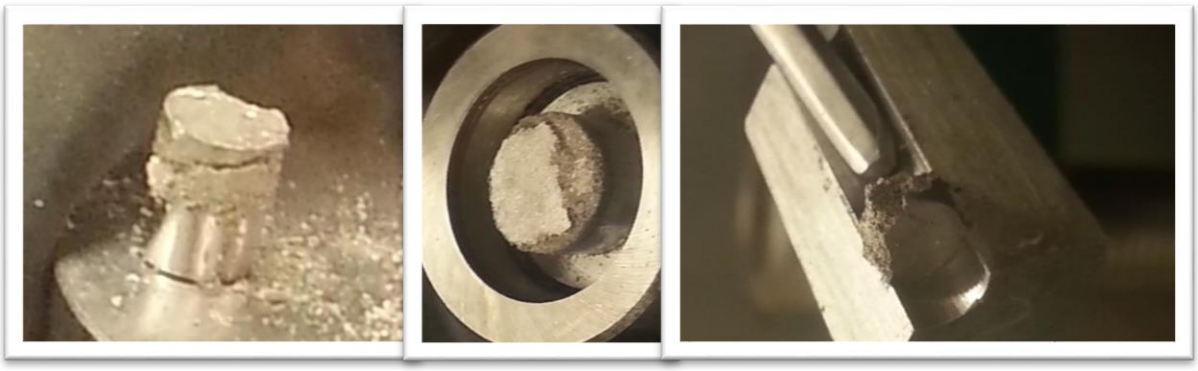

Figure 3-8: Examples of failed pellets

It was postulated that the act of pouring mixed powder into the die created stratification due to the differing metal densities and particle sizes and thus in-die mixing was utilized. A 5.5 millimeter aluminum stirring rod was designed and then attached to an all-thread rod by wire wrapping, pressing, and using a strong epoxy adhesive as shown in Figure 3-9. This rod was utilized after pouring and before pressing to ensure proper zirconium mixture. A few seconds of spinning the rod in the die proved adequate for mixing.

Figure 3-9: In-die stirring rod

To prevent splitting the pellets with the die, a ring was used as a pellet ejector and the pellet was gently pushed out of the die using the press. This required minimal force (i.e., only enough to make the needle jump slightly on the Mini-C pressure gauge, however pushing the pellet out by hand or gentle tapping on the push rod failed to release it from the die walls.

The pressing pressure was tested from 12,000 pounds force (~274 ksi, 1,890 MPa) down to 6,500 pounds force (~148ksi, 1,020 MPa) based on the procedure used by McDeavitt [25]. At the lower band, the pellets were too delicate and fell apart while extracting from the die or measuring. At the higher band, there was stratification of density producing a "gumdrop" shaped extremely dense core extending to the bottom or top and a loosely packed top or bottom on the other end as shown in Figure 3-10. The 8,000 pounds force (~183ksi, 1260 MPa) pressure produced the most consistent and homogeneous density observed in this experiment.

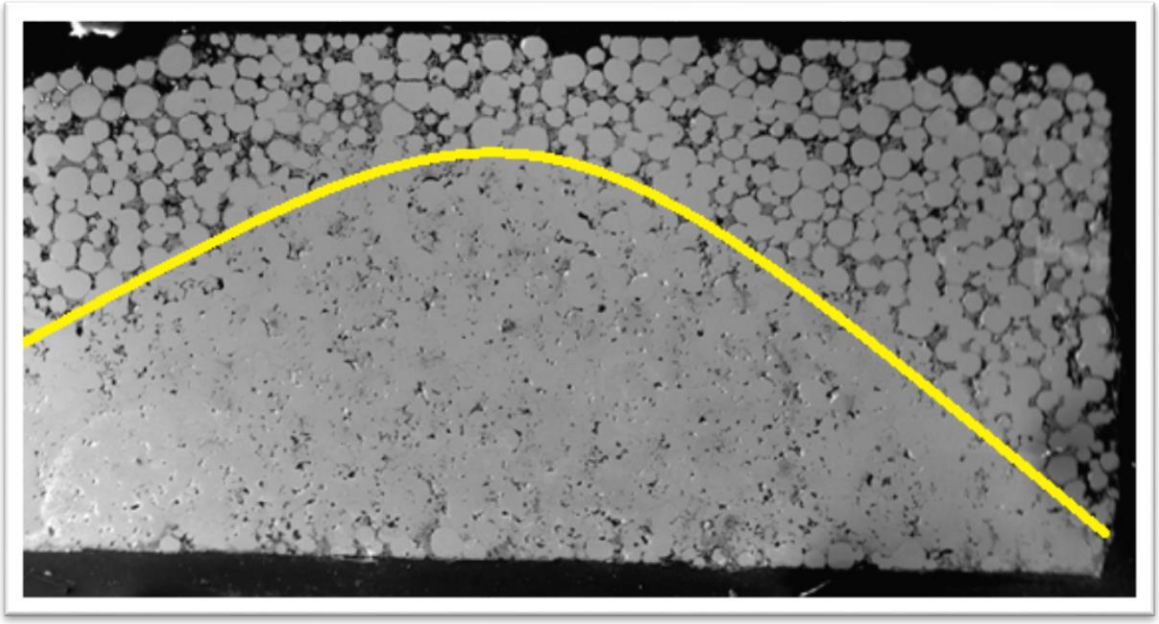

Figure 3-10: Example of stratification of density at high pressing pressure and the resulting "gumdrop" shape

After removal from the press, the diameter and height of each green pellet was measured three times from three different points approximately 120 degrees apart to increase accuracy. These measurements were then averaged and compared to the mass to determine density according to equation 3-1.

$$\rho = \frac{m}{V}, where V = \pi \times r^2 \times h \qquad 3\text{-}1$$

Where ρ is density in grams per cubic centimeter (g/cc), m is pellet mass in grams, and V is pellet volume in cubic centimeters as determined by the average pellet radius, r, in cm, and average pellet height, h, in cm. For the green pellets, porosity could then be determined by comparing this density to the theoretical density for the U10Zr mixture as

determined by the equation for density of mixtures as shown in equation 2-4 and equation 3-2.

$$\%P = 100 - 100 \times \frac{\rho}{TD} \qquad 3\text{-}2$$

Where %P is percent porosity, ρ is the dimensionally measured density of the pellet in g/cc per equation 3-1, and TD is the theoretical density of the pellet in g/cc (17.84 g/cc) per equation 2-4.

3.3 Sintering

A sintering furnace had to be constructed inside the glove box to facilitate this experiment. An inert atmosphere was vital to the process since the buildup of oxidation layers would prevent bonding and defeat the entire sintering process. This sintering furnace consists of a) a sintering tube designed to hold the sample, contain the controlled atmosphere, and protect external equipment from heat, b) a furnace housing to contain the furnace heater, protect glove box equipment from heat, and hold the sintering tube stable during operation, and c) accommodations needed to operate the system inside the glove box.

A 2" alumina tube was used for the containment body of the sintering rig. A steal head was constructed with 3 open penetrations and a 4th sealed penetration as shown in Figure 3-11. A high temperature rubber gasket was attached to the head and wrapped around the top of the tube to fully seal the enclosure. The sealed penetration contained a ¼" stainless steel tube with a notch ground into the top of the tube near the end in order to securely hold the wire suspending the crucible secure and prevent sliding. Two more

stainless steel tubes provide a gas inlet that reaches to the far side of the tube and a gas outlet near the head. A cover gas was required since the glove box only monitored oxygen and moisture levels. As discovered during initial tests, the glove box contained unknown levels of nitrogen that turned a test sample a golden color after sintering. There was the potential of other unknown gases that could react with the sample. Therefore, an ultra-high purity (99.995% Ar) argon cover gas was utilized. A thermocouple is the concluding penetration. Four stainless steel heat shields slide over the gas inlet, outlet, support tube, and thermocouple. These heat shields are separated by ½" copper tube spacers slid over the gas inlet line. The heat shields prevent overheating of the rubber gasket and further stabilize the stainless steel tubes and thermocouple.

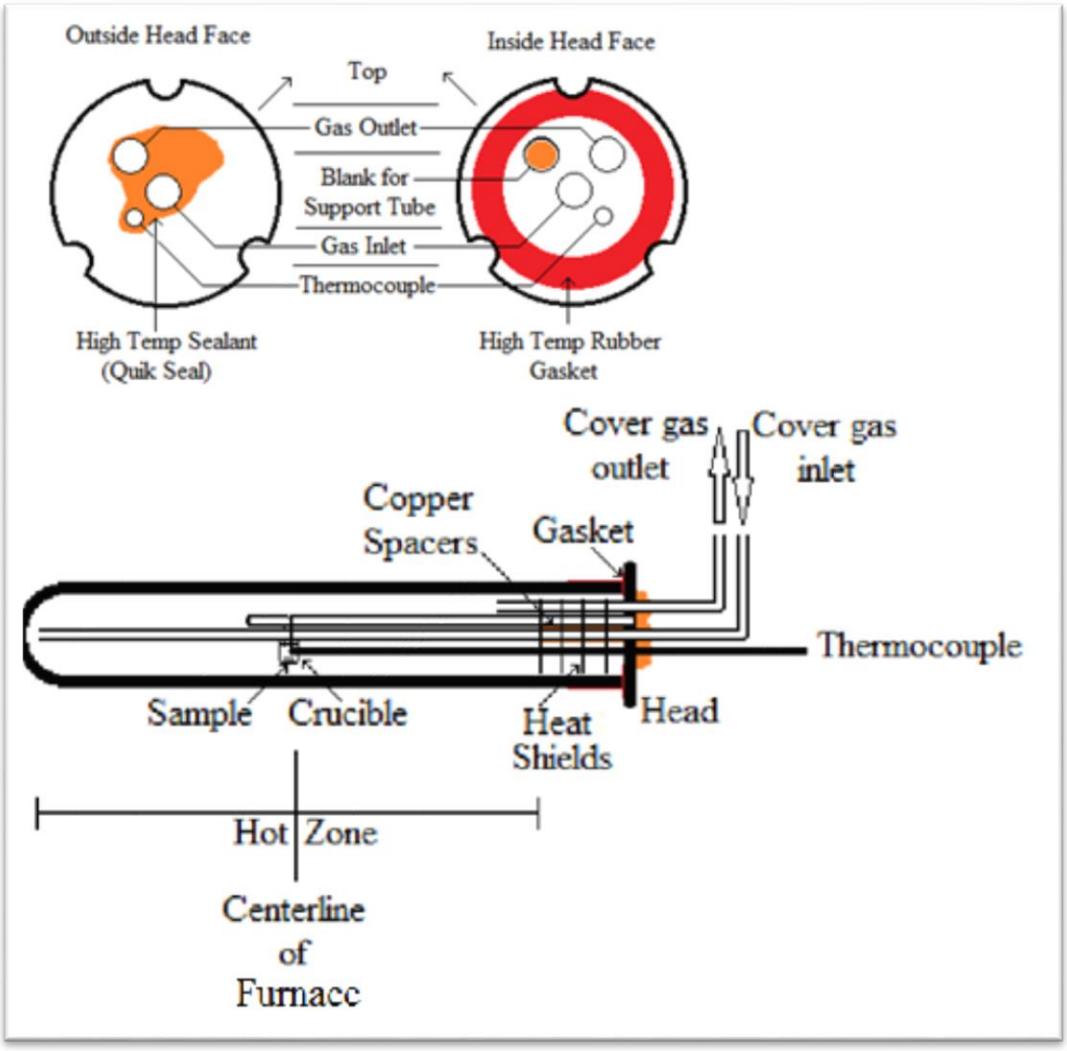

Figure 3-11: Sintering rig configuration

The crucible had to be constructed since an alumina crucible cannot be used with uranium and zirconium because these elements will oxidize while in contact with the alumina when heated. The crucible was made with a tantalum plate wrapped with a molybdenum mesh to form a basket. The mesh was then woven with a tungsten wire to keep it secure. The tantalum plate was slid into the basket and the bottom of the basket

was cut and folded closed under the plate to hold it in place. Another tungsten wire was woven into the basket to form a handle. Finally, a hole was punched into the molybdenum mesh so that the thermocouple end would rest directly above the sample during heating in order to provide the most accurate sample temperature during furnace operation as shown in Figure 3-12.

Figure 3-12: The constructed crucible rig with thermocouple inserted

In order to prevent any air leakage and revolving of the gas tubes or thermocouple during operation, a high temperature sealant RTV and Kwik Seal was applied in layers

to build up an external seal. Finally, a pipe clamp with three modified strut clamps was tightened around the outside of the external rubber seal. The modified strut clamps were bent around the pipe clamp with a bolt hole at the top so that a bolt could be inserted. Wing nuts were placed at the end of the bolts and these were used to tighten down on the head and accomplish a more airtight seal.

The furnace heater was a 6" inside diameter ceramic tube heater with a maximum heat capacity of 1200°C. Since the heater was much larger than the tube, four fire bricks were placed on both sides of the heater and a 2" hole was drilled between them. Fresh fiberglass rated up to 1260°C was wrapped around the outside of the heater and tucked between the fire bricks and heater faces. A hole slightly smaller than 2" was punched into the sides so that the insulation fit tightly around the furnace tube. The bricks were then wrapped temporarily in aluminum tape to compress the assembly while the heater performance was tested. Once heater operation was checked satisfactory, the aluminum tape was removed and the fiberglass wrapped furnace and fire bricks were lowered into a furnace box assembly that consisted of aluminum angle bars, aluminum straight bars, four all-thread rods, and stainless steel plates. The aluminum angle bars covered the 12 edges of the box. The four aluminum straight bars pressed and held the fire bricks in place while preventing rubbing against the associated angle bars, thereby reducing wear and tear on the fire bricks. The stainless steel plates covered the four faces of the box that didn't have fire bricks and distributed any lost heat from the insulation, especially on the bottom because of compression. The bolts on the all-thread were tightened to snuggly compress the fire bricks, insulation, and heater together and thermally seal the

inside of the heater tube for better heat retention. Used fiberglass insulation bits were then packed into the free space of the box to further seal the box from heat loses. The heater wires were electrically and thermally insulated to prevent any damage. The testing of the heater and final construction before moving into the glovebox are shown in Figure 3-13.

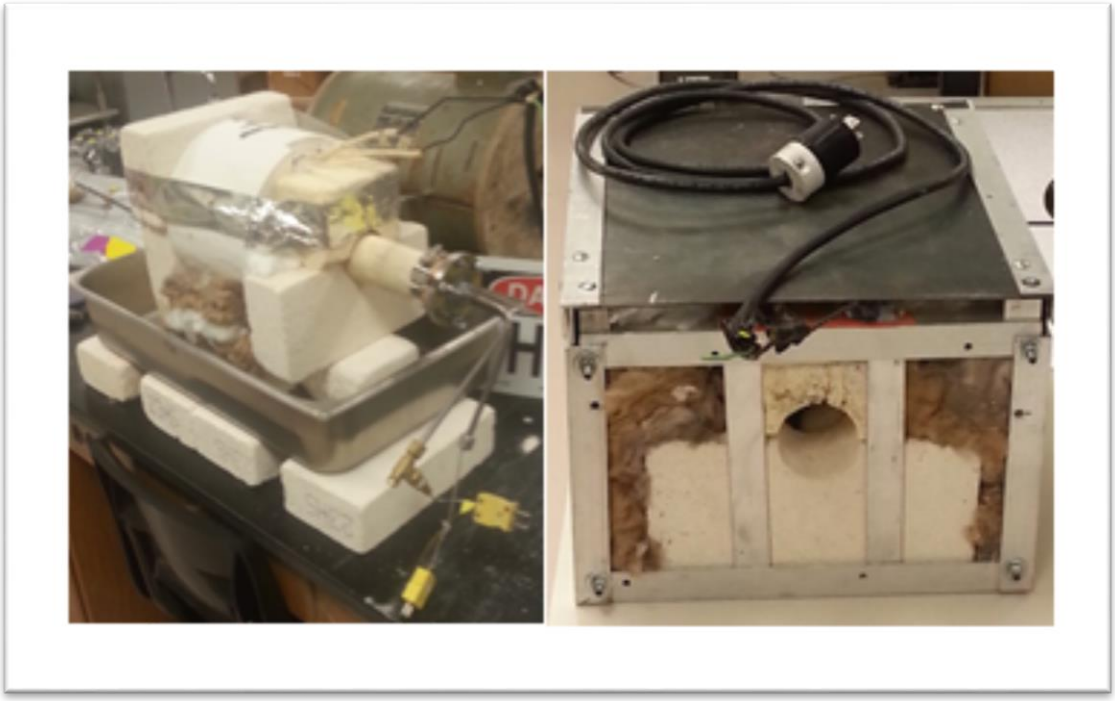

Figure 3-13: Sintering furnace before assembly (left) and in housing (right)

The furnace assembly proved to be less than an inch too wide for the largest antechamber. Because of this, the furnace was partially disassembled and moved into the glove box in pieces and then reassembled inside. The furnace pieces were left in the

glove box antechamber to off gas for 24 hours before transferring in due to the porosity of the insulation and complex nature of the structure. In order to protect the glove box floor and seals, the furnace was propped up on strut channels. The furnace was centered in the glove box to protect gloves and window seals. High temperature warning signs were added to the glove box to warn users not to touch the furnace during operation. An electrical plug was already present in the glove box for the heater to receive power. However, there was no penetration in the glove box for the thermocouple connection. A Conax connection has to be installed in the top of the glovebox. One such connection was removed from an old assembly on another glove box and modified for two thermocouple connections (in case one failed during operation). A furnace controller was selected and mounted under the glove box. This controller was a Watlow SD series PID controller mounted in a relay box built by Thermal Solutions Controls & Indicators LLC. The controller was limited by design to a maximum of 1000°C. Since there was a lag in the controller measured temperature (usually less than 10°C) and for the purpose of protecting the silicon seals in the glove box, the temperature was limited to 900°C. The ultra-high purity argon line attached to the TIG system was tapped into between the outlet of the secondary flow gage and the inlet to the TIG welder, run into the glove box, and into the sintering rig. This line supplied the cover gas to the sintering tube. The gas outlet was allowed to vent into the glove box and as long as continuous flow was established no back flow was expected. A line was attached to the glove box so that an external vent with a bubbler could be used, but was only tested and was never utilized for these experiments.

During final testing, the sintering furnace emitted large amounts of oxygen as indicated by the glove box oxygen monitoring system. Oxygen increases of over 100 parts per million (ppm) were observed. This proved that the off gassing procedure was inadequate. This threatened to oxidize the pellets while sintering and possibly defeat the entire sintering process all together. To remedy this, the sintering tube was loaded into the furnace, with the crucible, and the heater controller was set to the maximum 1000°C to force a more complete off gassing. The ultra-high purity argon cover gas was used to maximize oxygen removal. The furnace was operated this way for over 24 hours. A second test run was started and once again glove box oxygen levels increased, except this time it was less than a 40 ppm increase in the glove box. For this reason, the furnace off gassing was allowed to continue over a weekend adding an additional 60 hours of off gas time. During this time, the glove box silicon seal were checked frequently and no damage occurred. The subsequent run following this procedure produced a less than 10 ppm increase in oxygen in the glove box for a short time during the heat-up cycle and reduced back to normal levels before the desired temperature was achieved. All runs after this had only minor to no increase in glove box oxygen levels.

A basic heater or furnace cycle consists of three steps: ramp up, soak, and cooldown. Ramp up is simply the process of heating to the desired temperature with a controlled rate: the ramp rate. Soak is the time period at which the desire temperature is held constant to accomplish the task this cycle is performing (sintering, annealing, heat treating, etc.). Cooldown is the same as ramp up just in the opposite direction. Some ramp up and cooldown cycles are performed in steps to increase the speed of the cycle

while not endangering the object being heated. Some objects require multiple soak times and temperatures depending on the purpose of the cycle.

The controller ramp rate was tested. It was initially set at 200°C/min and the units for this were not explicitly indicated on the controller or in the manual. This resulted in cracking of the initial alumina tube which was quickly replaced. Ramp rates between 50 and 8°C/min were tested, but a final 10°C/min was settled on for ease of estimating time till desired temperature is achieved, to reduce the lag between temperature set point and indicated temperature, and less cycling during the end of the ramp up. The controller offered no cycle control and was completely manual. For this reason, the temperature had to be set, the system monitored during operation, and the temperature had to manually be dropped to zero for the controlled cooldown process to begin.

For the experiment, freshly pressed pellets were loaded into the crucible. The crucible was carefully slid so that the thermocouple end rested directly above the pellet in the center of the crucible and the "handle" of the crucible rested on the grove of the support tube. The sintering rig was then carefully slid into the sintering tube while maintaining the cover gas lines directly up the entire time (they were aligned this way during construction of the head to ensure the crucible basket wasn't swung while mounting the head on the tube). The mounting bolts aligned with the three notches in the head. Wing nuts were placed on the bolts and tightened down to ensure compression of the rubber gasket on the inside of the head. The cover gas supply line was given excessive slack and remained on the head between experiments as to limit leaks and reduce the amount of tools needed to operate this system. The tube was then carefully

loaded into the furnace. The back side of the furnace was blocked with insulation and the tube didn't protrude out of the back. A mark was made on the tube to indicate were the tube should stop at the opening at the front of the furnace. This mark was based off the furnace depth of 6" measured after the compression of the furnace housing. It insured that the crucible set at the centerline of the furnace. It also ensured that the heat shields inside the tube were outside of the furnace and adequately protected the rubber seals and head. An additional piece of insulation was placed around the front opening to increase thermal retention and protect the tubes and wires. The thermocouple wire was then connected and safety signs mounted. The controller temperature was set, cover gas flow was established, and time noted. Cover gas flow was maintained at just above minimum detectable flow in the secondary flow gage (less than 2 standard cubic feet per hour equivalent air). Since a temperature of 900°C was desired, it was discovered experimentally that a set point of 905°C was necessary on the controller to maintain this temperature on the thermocouple during the soak time. The expected time for soak to start was calculated and used to ensure the programmed ramp rate was performing as it was supposed to. Five minutes before the expected time to soak was achieved, the controller was checked. In all instances, the measured temperature was above 895°C (typically between 897 and 900°C) at the expected time to soak. This time was marked as the beginning of soak and the furnace was checked periodically for temperature stability, cover gas flow, and changes in atmosphere as indicated on the glove box controller. Once the desired sintering/soak time was achieved, the controller temperature was lowered to zero. The cool down rate used was the same as the ramp up

rate on this controller, however, because of the excessive insulation, the system typically lagged behind the controller for cool down and the tube was pulled out of the heater slightly below 300°C to facilitate faster cooling (the controller was typically off already by this time).

The pellet was then removed, visually inspected, and measured. Typically, a small amount of oxidation was noted in the form of blackening around the circular edges of the pellet. The pellet was then weighted in order to determine any mass changes and then measured for volume in the same manner as the green pellet.

3.4 Polishing

The purpose of polishing is to provide a flat, scratch free surface for accurate SEM imaging while exposing the surfaces of interest for the experiment. This was accomplished using both manual hand polishing and automatic polishing. Hand polishing was performed with sandpaper, purified water, and a metal tray for containment. Automatic polishing was executed with a Buehler MiniMet 1000 grinder-polisher as shown in Figure 3-14 [reprinted from 26]. Purified water was used as the lubricant for polishing.

Figure 3-14: The Buehler MiniMet 1000. Reprinted from [26]

In order to prepare for polishing, the sintered pellet was mounted in a cylindrical epoxy mold. After the mold dried, the pellets were cut to expose the axial, or transverse, face and then one side polished to expose the radial face near the center as shown in Figure 3-15. The cutting was accomplished using a Leco VC-50 Precision Diamond Saw as shown in Figure 3-16 [reprinted from 27]. One of the two halves was then marked for polishing. Half of the measured height was marked into the epoxy mold. A caliper was set to half the height and then gently pinched so that it would not slide. The

lower jaw was placed on the edge of the bottom of the epoxy mold and the top edge of the upper jaw was used to etch a line around the mold. This half was then taped back to the other half with the other half flipped so that the pellet side was face up. The mold was then polished to penetrate up to the etched line, exposing the center of the radial face as shown by the middle picture in the above figure. This was accomplished by hand and consisted of using sandpaper grits 180, 240, and 400. The progress was monitored by vision and thus the times and amount of pressure used varied per grit. In general, the 400 grit sandpaper was used the longest to clean any surface damage from the lower grits.

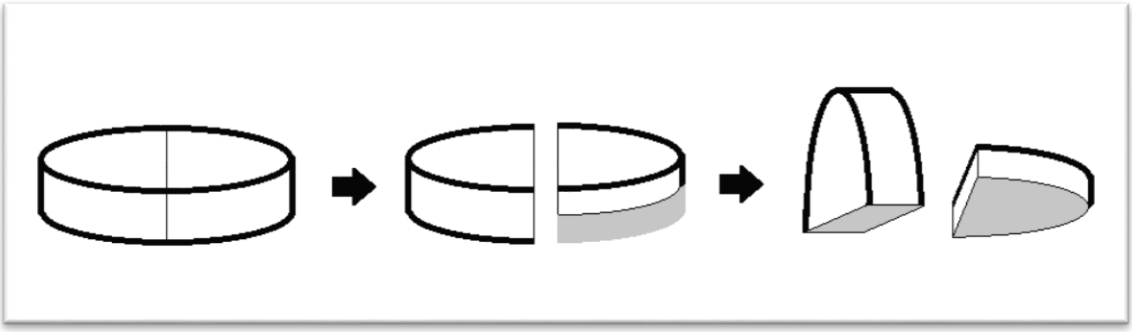

Figure 3-15: Cutting and polishing schedule for pellets

Figure 3-16: The Leco VC-50 Precision Diamond Saw. Reprinted from [27]

Once the radial face was penetrated deep enough, the Leco diamond saw was used to trim the epoxy mold around the radial and axial faces. These mold blocks were then thoroughly cleaned with ethanol, sonicated, and placed into a new epoxy mold with the appropriate faces faced down. A stainless steel ring was added around the samples for the purpose of preventing rounding of the bottom face of the mold while polishing. Originally, copper rings were used but they proved to be too soft and copper particles came loose while polishing which scratched the samples and lodged in the epoxy. A stainless steel ring replaced the copper and balanced the mold face therefore preventing rounding without damaging the samples. Once the final epoxy mold dried, the back side of the mold was sanded by hand to remove the meniscus formed by the liquid epoxy. The number of the sample was then etched into the back side of the epoxy to identify the

sample. The final step in polish preparation was to use hand polishing with 400 grit sandpaper on the bottom face of the mold to remove any epoxy formed below the sample faces. This arrangement is shown in Figure 3-17.

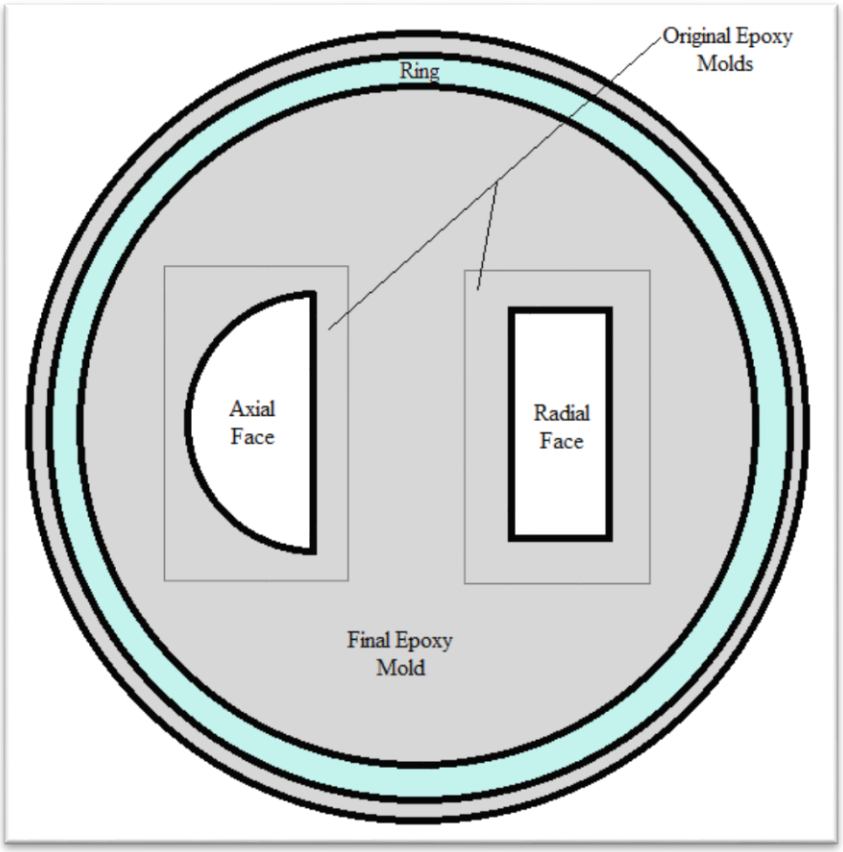

Figure 3-17: Final sample mounting

Samples were then ready for automatic polishing. In order to track and improve polishing methods, an initial polishing schedule was developed based on stainless steel polishing from Jordan Evans [28] and modified slightly as shown in Table 3-1. The

modified values are the first three, hand polishing steps early on.

Table 3.1: Initial planned polishing schedule. Reprinted from [28]

Grit	Method	Time	Pressure	Speed
320	Hand	As needed	As needed	30 if on Mini-Met
400	Mini-Met/Hand	30 min	0 N	30 if on Mini-Met
600	Mini-Met/Hand	30 min	0 N	30 if on Mini-Met
800	Mini-Met	30 min	0 N	30
1200	Mini-Met	30 min	0 N	30
3μm susp	Mini-Met	30 min	0 N	30
1μm susp	Mini-Met	30 min	0 N	30
0.5μm susp	Mini-Met	30 min	0 N	30
0.05μm susp	Mini-Met	30 min	0 N	30

Beginning with these recommendations, actual polishing times were carefully logged in the first two samples. The initial polishing schedule proved inadequate and required back-stepping multiple times around 1200 and 800 grit to remove scratches. Additionally, increasing speed a little at the higher grits vastly improved the progress and cleaning of the surface. It was also determined that the 0.5 micron and 0.05 micron suspensions were not necessary for final finishing. The average actual times are shown in Table 3-2. The entries in Table 3-2 are not chronological and represent total time. For instance, the 3μm suspension fluid was used in 30 minute integrals and then verified in an optical microscope. If the sample was still scratched, polishing continued back at 1200 grit. Typically, until 1200 grit, the sample was verified visually with the naked eye. After the 1200 grit and the suspension fluids, the sample was moved to an optical microscope to ensure the surface was truly scratch-free.

Table 3.2: Actual initial polishing times

Grit	Method	Time	Pressure	Speed
Prep:180	Hand	90	Moderate	N/A
Prep:240	Hand	60	Light	N/A
Prep:400	Hand	90	Light	N/A
Prep:400	Hand	30	Moderate	N/A
400	Mini-Met	30	0 N	30
600	Mini-Met	60	0 N	30
600	Mini-Met	30	0 N	35
600	Mini-Met	30	1 N	35
800	Mini-Met	30	0 N	30
800	Mini-Met	120	0 N	35
800	Mini-Met	60	1 N	35
1200	Mini-Met	120	0 N	30
1200	Mini-Met	150	0 N	35
1200	Mini-Met	60	1 N	35
3μm susp	Mini-Met	120	0 N	35
1μm susp	Mini-Met	30	0 N	35

Analyzing the actual polishing data, a final polishing schedule was developed for each sample, with only minor modifications afterward. It was noticeably necessary to increase the aggressiveness of polishing in the 600, 800, and 1200 grit ranges since these were the ranges in which back-stepping was required. Increasing the speed in the higher ranges proved beneficial but in the lower grit ranges, it caused the polishing arm to jump. Increases the polishing pressure worked best in the middle of the grit ranges; at the smaller grits it caused the arm to jump also and at the higher grits it showed no improvement of performance. Therefore, based on the experiences in this experiment, the final polishing schedule for U10Zr pellets was developed as shown in Table 3-3. Steps I through III are the preparatory steps performed after initial cutting in order to expose the center of the axial face. Step IV is the preparatory step after final mounting

used to remove any epoxy formed on the faces of the sample. Steps 1 through 8 are the final polishing steps. Typically, the only variation necessary involved increases either the time or pressure at step 6 to either 45 to 60 minutes or 2 Newtons. Additionally, to improve cleaning of the sample surfaces during polishing at steps 5 through 8, the polishing dish was inundated with purified water once the timer on the polisher was on the last minute or two of polishing. The polishing plate and bowl were cleaned thoroughly between each step with ethanol and shop towels. The sample was sonicated in ethanol between each step and patted dry with a shop towel.

Table 3.3: Final polishing schedule

Step	Grit	Method	Time (min)	Pressure	Speed
I	180	Hand	As needed	Light-Moderate	N/A
II	240	Hand	As needed	Light	N/A
III	400	Hand	As needed	Moderate	N/A
IV	400	Hand	As needed	Moderate	N/A
1	320	Mini-Met	30	0 N	30
2	400	Mini-Met	30	0 N	35
3	600	Mini-Met	30	1 N	35
4	800	Mini-Met	30	1 N	35
5	1200	Mini-Met	30	2 N	35
6	1200	Mini-Met	30	1 N	35
7	3μm susp	Mini-Met	30	0 N	35
8	1μm susp	Mini-Met	30	0 N	35

3.5 SEM Imaging

SEM imaging uses a focused beam of electrons to produce a topographical image. The electrons interact with atoms releasing secondary electrons, backscattered electrons, and characteristic photons which the device can measure. These photons and electrons

coupled with the beam emitter location provide a surface image of the sample with element compositional information. The SEM method utilized measured backscatter electrons in a high vacuum.

In order to prepare the sample for the SEM, the epoxy mold had to be carbon coated. A Cressington 108C Auto Carbon Coater was used to accomplish this. Once the sample was sonicated following final polishing, it was inserted into the auto carbon coater. A vacuum was drawn in the coater chamber and the unit energized to sputter coat the sample with carbon. A few seconds after the first sputter was completed, a second sputtering cycle was initiated. The sample was then removed and transferred to the SEM.

The SEM has its own mounting block which the cylindrical epoxy mold slid into. The sample was then tightened into the mounting block by screwing in the set screws. Copper tape was then added across the epoxy. This tape attached the mount to the epoxy electrically and improved image resolution by providing a shorter path for electrons to the sample. The sample was then loaded into the SEM chamber and vacuum drawn to below 5.0×10^{-6} Torr.

Once vacuum was achieved the desired level, the SEM was energized and imaging began. The basic images required were 25x magnification of both faces, 100x magnification scan of both surfaces, a 200+x magnification of specific features such as alloying, artifacts, and pore formations, and finally a composition map. Using Energy Dispersion Spectroscopy (EDS), the SEM can provide compositional information. This was performed at the 100x magnification and smaller to denote certain features. The

working distance and current were recorded for each image.

3.6 Image Analysis

Multiple methods of surface image discrimination were used to verify the results of the image including binary, 8-bit color and grayscale, 16-bit color and grayscale, and full color threshold analysis. Since most methods produce very similar results, except for binary which was discarded, and for simplicity of reporting, full color threshold analysis was used for comparison to dimensional measurements and actual density measurements.

SEM images output with a 2048x1526 pixel resolution. At 50x magnification scale, the resolution in ImageJ proved to be too low and much of the porosity was difficult to isolate and differentiate from other features. This produce very high densities. Because of this, the 100x magnification image scans were utilized. The bottom 38 pixels were removed to eliminate interference from the SEM imagining information (scale, voltage, and magnification). Furthermore, these individual images were parsed into a four by three grid, producing 12 new images at approximately 512 x 498 pixel resolution. This made fine tuning the thresholds much easier as most details could be seen with the naked eye without changing the zoom. Finally, if one of the new parsed images contained empty space due to being adjacent to a sample boundary, a rectangular section of the sample image was measured such that area was maximized while reducing error due to measuring at the boundary. An illustration of how this was accomplished is shown in Figure 3-18. The surrounding black box is the area being measured. The grey grid

shows how the black area was divided. The red bars and red X's in the top right are examples of the sections not measured near a boundary. Below the black box, where the SEM image data is, was also not measured. All other surfaces were measured and logged.

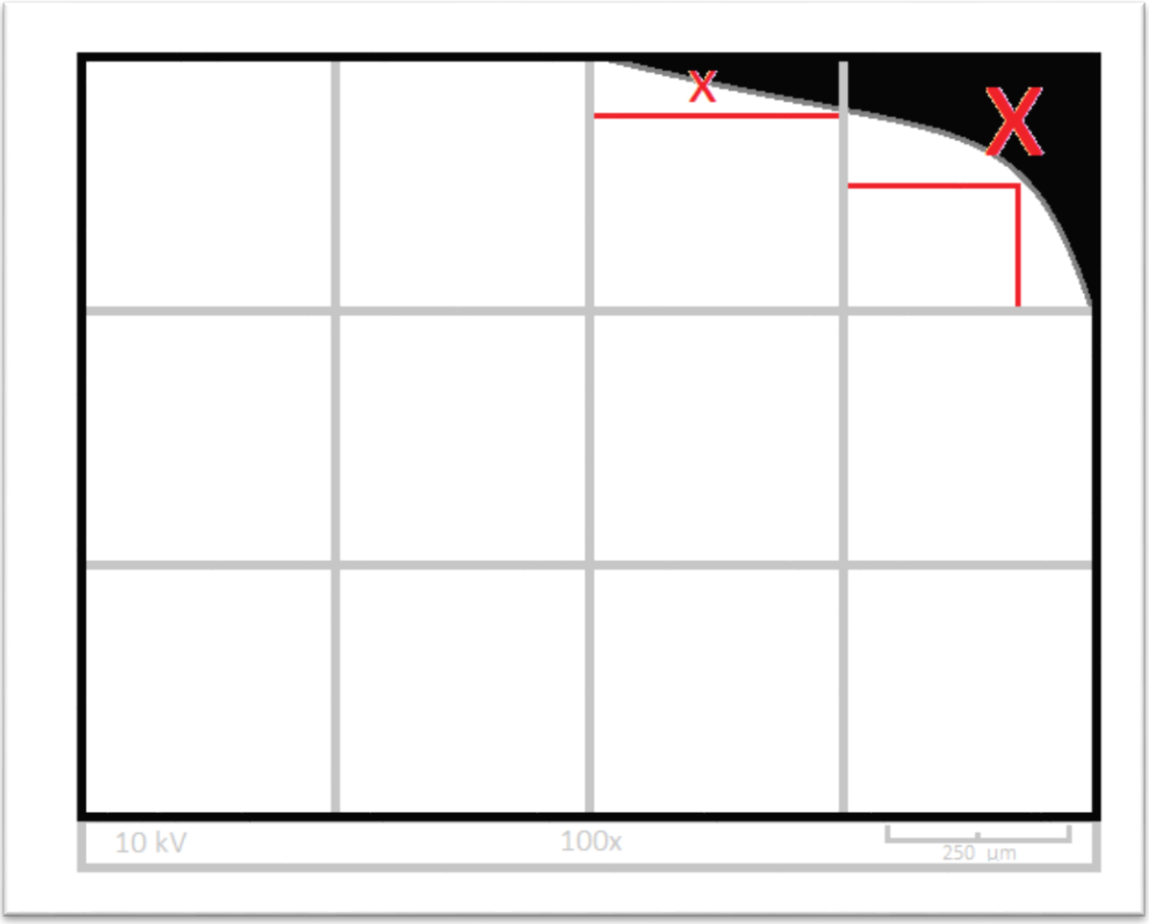

Figure 3-18: SEM image parsing

The first and primary image analysis method was surface area analysis. The resulting area fraction provides the percent porosity after sintering. This percentage can be used

to help determine the densification since the amount of alloying is an unknown. This analysis is accomplished through the ImageJ "% Area" function and discriminated with the upper and lower threshold for brightness. The lower threshold is left at the minimum (pure black) and the upper threshold is adjusted. Adjustment of the threshold is based off of the lower atomic mass impurities, zirconium enriched areas, and porosity. The threshold was lowered to exclude all zirconium areas. Lower mass impurities (such as carbon, silicon, etc) became trapped in some of the open pores at the surface during polishing and preparation. Since almost all impurities were occupying pore space, the threshold was adjusted to include as much as possible of these impurities. In some instances, the lower threshold for zirconium, especially samples that had begun oxidizing, closely overlapped the upper threshold for impurities. In these cases, the threshold was adjusted to exclude all zirconium regions.

Additionally, the change in porosity shape is also of interest. This provides a qualitative indication of sintering progress. This is indicated by the roundness and average pore size. ImageJ provides a measure of roundness using the "Circularity" and "Roundness" analyses under the "Shape Descriptors" function. Roundness provides a simple ratio of how well each pore fits into a perfect circle and is calculated by dividing the particle area by the product of pi, the longest, and shortest axis while circularity takes in account the object perimeter. It does this by dividing the area by the perimeter squared. Because of this, circularity provides a better indication of how smooth each pore is. The average pore size can be determined by the "Average Particle Size" function.

4. RESULTS

The results of this experiment include the production of powder, the production of pellets, and the analysis of the resulting pellets. Section 4.1 covers the results of pellet production before sintering. Section 4.2 describes the results of pellet production after sintering. Finally, section 4.3 describes the results of image analysis and compares these results to section 4.2 physical measurements.

Section 4.1 Pellet Pressing Results

Table 4.1 contains the results from the ten most notable pellets. The first three were the test pellets for determining the pressing procedure. The fourth pellet was the first produced with a standard procedure. Pellets five through ten produced successful, homogeneous, finalized results in all three category of results. The first pellet was not measured with calipers due to many failed attempts prior where pellets had crumbled while attempting to press and measure. Pellets two and three were used to find a pressing procedure that produced homogeneous and stable green pellets. Pellet four was the first stable pellet, however it was not hot homogeneous as discussed in section 3.2. Pellet ten replaced the results for pellet four.

Table 4.1: Pellet pressing results

Sample	Pressure	Time	Mass	Volume	Density	% TD
	lbf	sec	g	cc	g/cc	
1	12,000	60	1.86	*	*	*
2	12,000	60	1.72	0.109	15.71	88.0
3	10,000	60	1.02	0.083	12.30	68.9
4	8,000	60	1.10	0.072	15.32	85.8
5	8,000	60	1.13	0.086	12.96	72.6
6	8,000	60	0.98	0.073	13.39	75.1
7	8,000	60	0.75	0.069	10.90	61.1
8	8,000	60	0.82	0.069	11.90	66.7
9	8,000	60	0.96	0.064	15.02	84.2
10	8,000	60	0.92	0.073	12.67	71.0

*Pellet was too fragile and sintered without measuring

Section 4.2 Pellet Sintering Results

Table 4.2 contains the results from sintering. Since the initial pellets were for refining the procedure, the second and third pellets were not measured after sintering. By pellet four, each was measured to check for densification.

Table 4.2: Pellet sintering results

Sample	Temp	Time	Ramp Rate	Mass	Volume	Density
	Celsius	hrs	C/min	g	cc	g/cc
1	900	12	400	1.85	0.133	13.92
2	900	12	12	*	*	*
3	900	12	10	*	*	*
4	900	12	10	1.08	0.079	13.67
5	900	10	10	1.13	0.085	13.27
6	900	8	10	0.98	0.072	13.48
7	900	6	10	0.75	0.066	11.38
8	900	4	10	0.81	0.068	12.04
9	900	2	10	0.95	0.068	14.10
10	900	12	10	0.92	0.072	12.82

*Measurement not taken

Section 4.3 Image Analysis Results

The first three pellets were analyzed under an optical microscope before SEM imaging to ensure polishing quality. Figures 4-1 through 4-3 show optical results for pellets one through three respectively. As evident in fig. 4-1, pellet one had a laminar separation during pressing due to sticking to the wall. Pellet two suffered from a large stratification in density which resulted in a large amount of pull-out during polishing and a large chunk removed during cutting. In fig. 4-2, the left image shows the knocked out area and both images show the large amount of pull out and stratification. Pellet three showed much improvement in stratification and stability. However, as evident in fig. 4-3, pellet three still suffers from slight knock-out during polishing and cutting. Additionally, pellet three suffered from uneven polishing. The copper ring used to improve polishing results was installed on all pellets following this one.

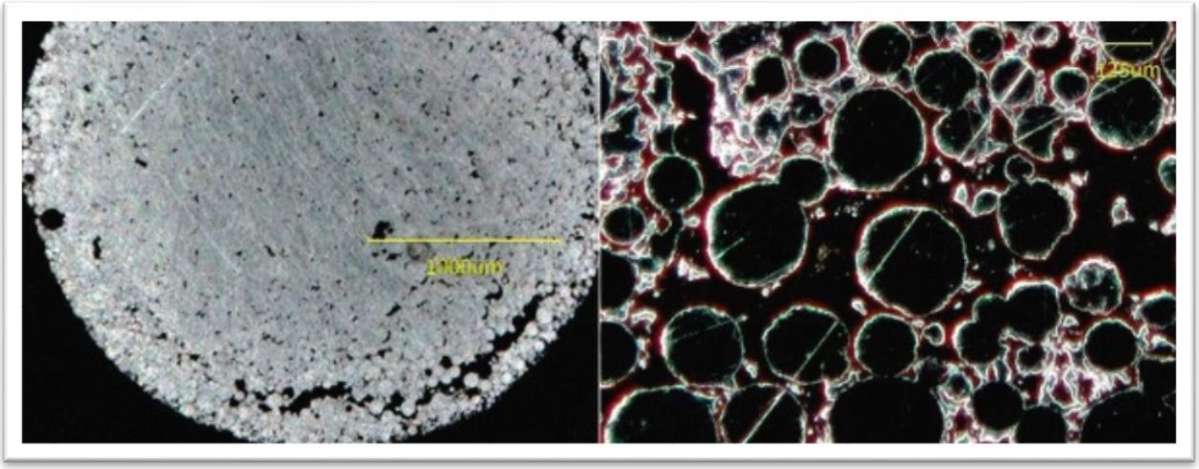

Figure 4-1: Optical imaging of pellet one

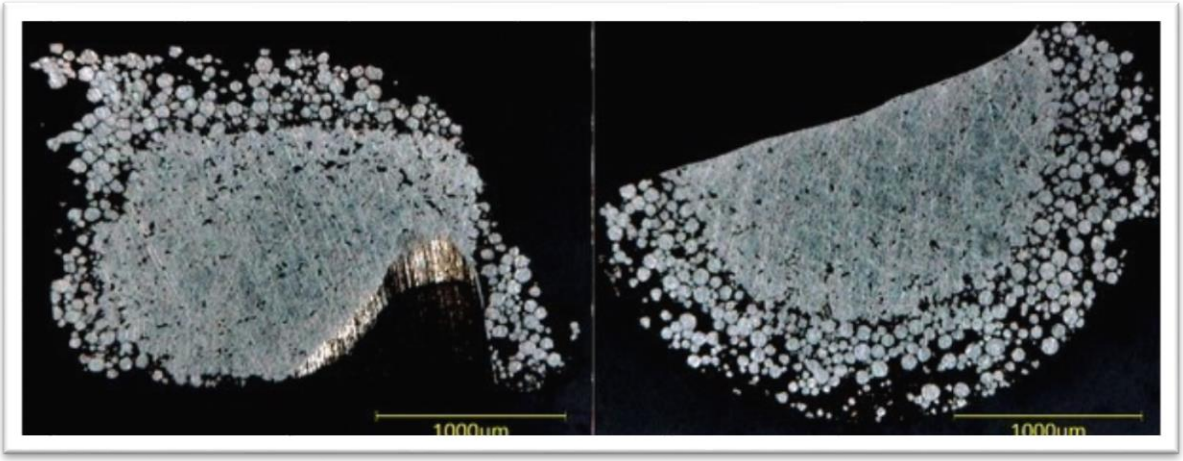

Figure 4-2: Optical imaging of pellet two

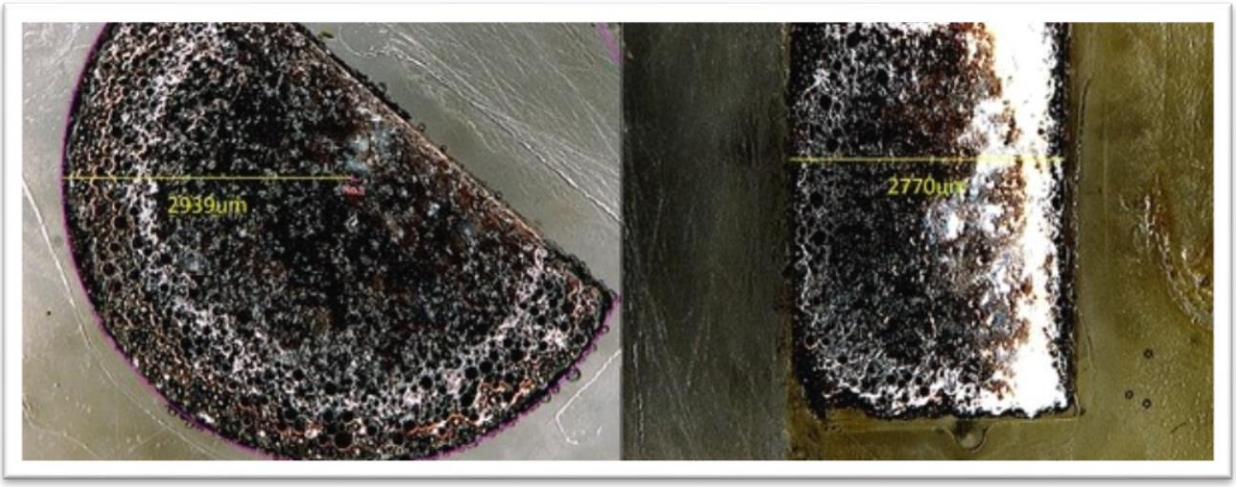

Figure 4-3: Optical imaging of pellet three

Once pellets were successfully sintered and polished, they were imaged in an SEM as discussed in the previous chapter. Figure 4-4 shows the results of the laminar separation, left image, and the high density center region, right. The outer region shows very little alloying between the uranium and zirconium. The darker zirconium areas in this region show little to no gradient indicating uranium diffusing into the mass. The high density region shows zirconium "rings" in the right image. Additionally, there are very few zirconium rich regions indicating thorough alloying.

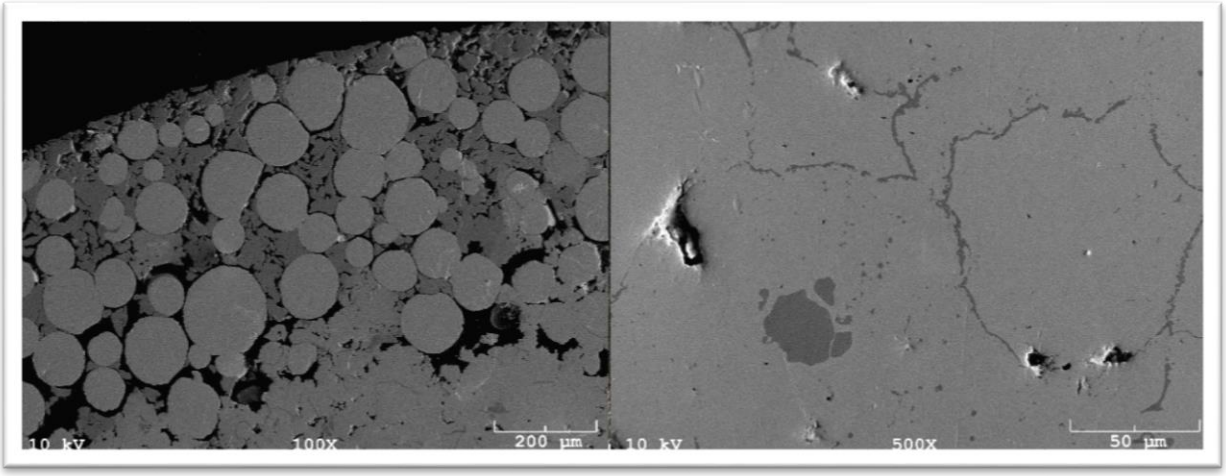

Figure 4-4: SEM imaging of pellet one

SEM images in Figure 4-5 show better detail of the peripheral pull out on the left. The interior has increased porosity from the first experiment, however the same zirconium "rings" still exist and even less zirconium rich zones exist. An additional artifact existed in pellet two; an area of porosity formed in the diffusion region in some peripheral areas. Figure 4-6 shows one such affected region which becomes noticeable at higher magnifications. These regions existed near large missing chunks from the cutting process knock-out. Additionally, a composition map was performed in the high density area in pellet two to check for impurities. Figure 4-7 shows the images and results from this composition map. Uranium is concentrated throughout. Zirconium is dispersed with small concentrated areas in the "rings" and small areas. Small amounts of silicon deposited in large pores. Oxygen was found dispersed almost uniformly throughout. No other elements were tested on this sample.

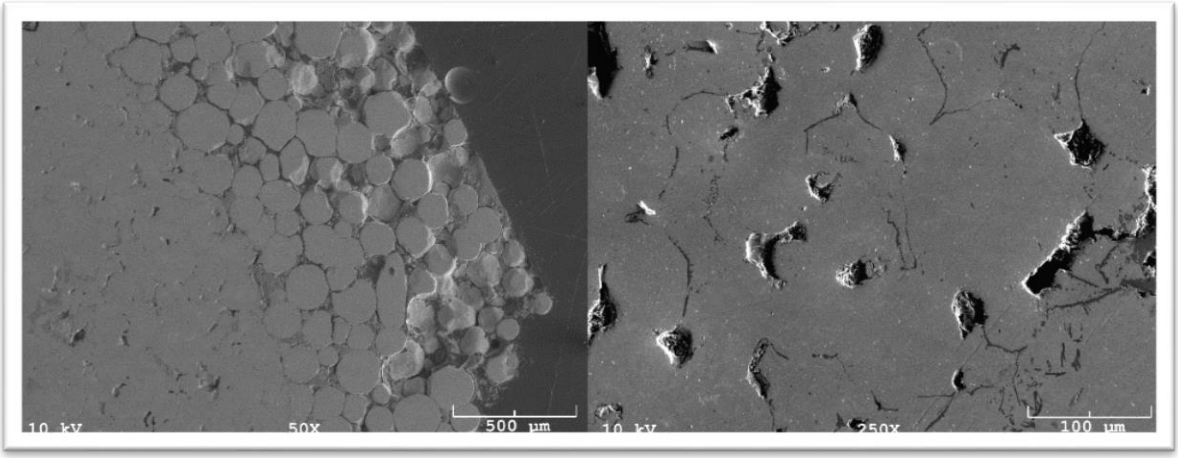

Figure 4-5: SEM imaging of pellet two

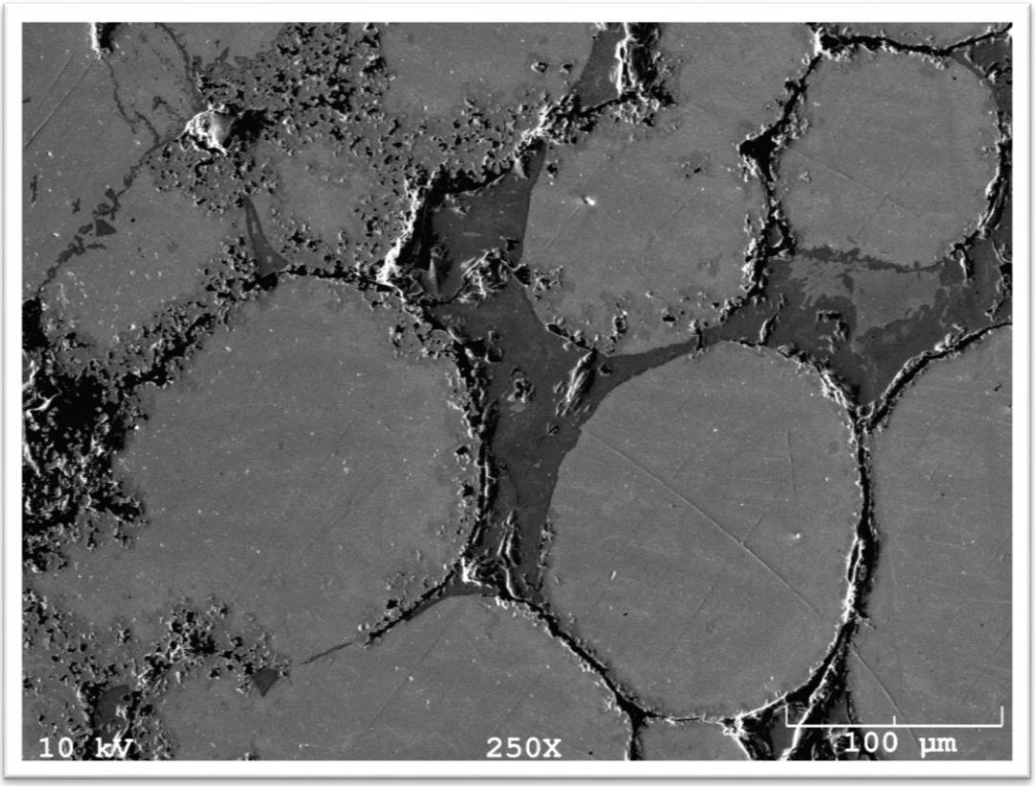

Figure 4-6: Pellet two peripheral diffusion porosity

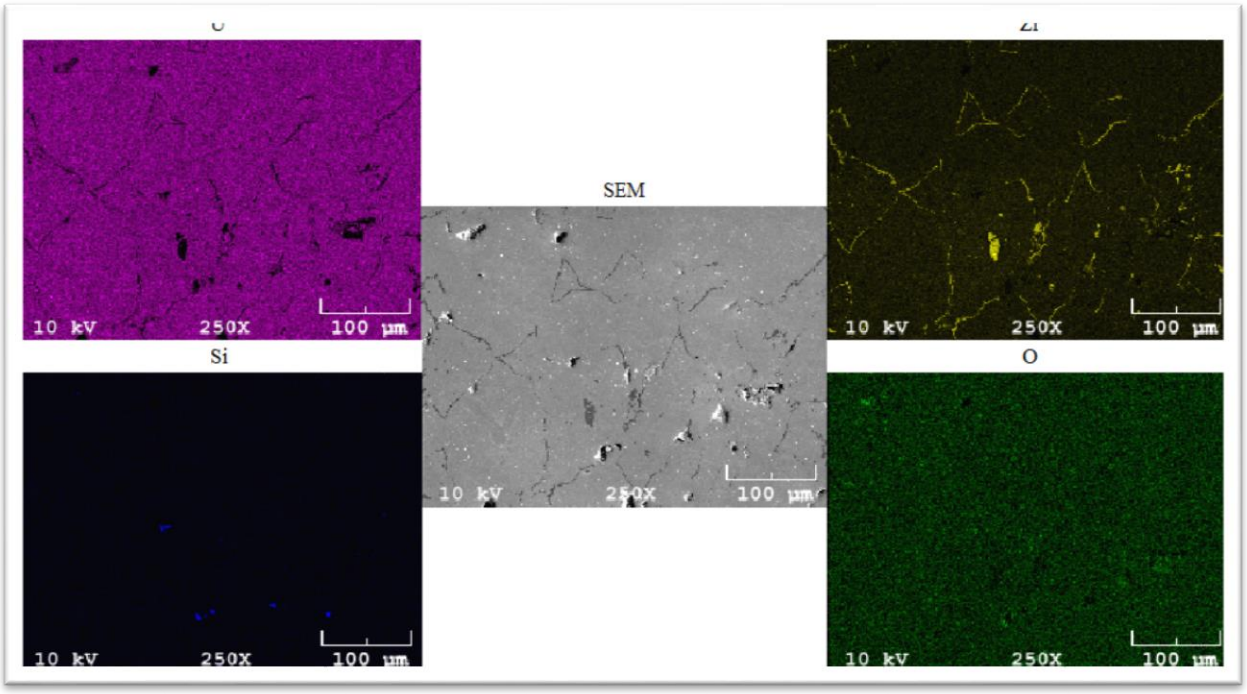

Figure 4-7: EDS map of pellet two

In Figure 4-8, the SEM images confirm the more homogeneous porosity and alloying in pellet three. A peripheral region still exists where alloying is occurring at a different rate. Additionally, as noted across the interior of the left image and in the top right of the right image, streaks or strands of a high contrast material appeared in various positions within the pellet. The compositional mapping, as shown in Figure 4-9, shows that these streaks are rich in carbon, nitrogen, and oxygen. This is likely caused by epoxy that had penetrated into the pellet so deep that polishing hadn't removed it. Once again, silicon was found trapped in large pores. Except for the epoxy ribbons, uranium is well dispersed. Zirconium is also dispersed with concentrations near pores and once again around the original uranium spheres. Additionally, nitrogen in the glovebox was

identified as a possible contaminant and this step is where a cover gas was installed to further control the sintering environment.

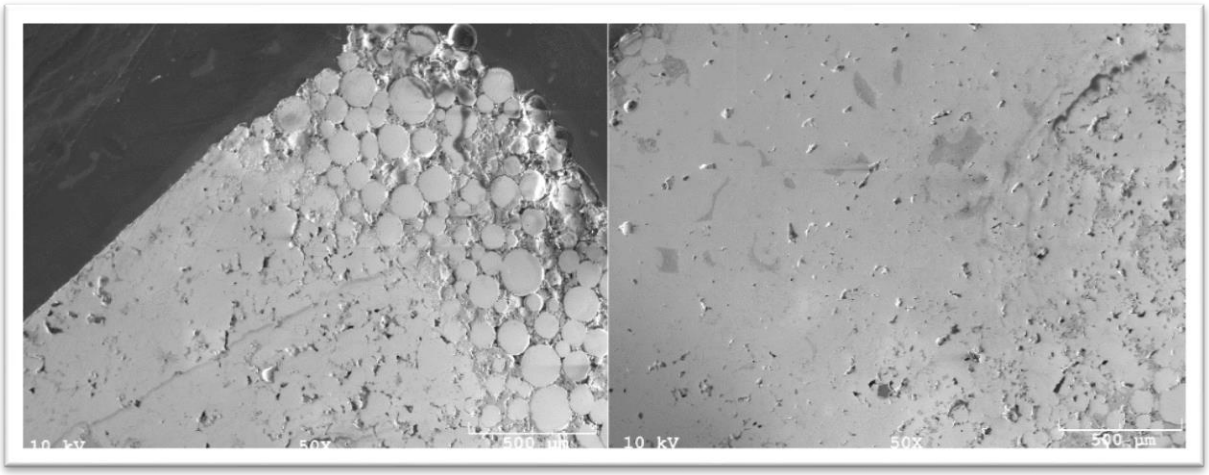

Figure 4-8: SEM images of pellet three

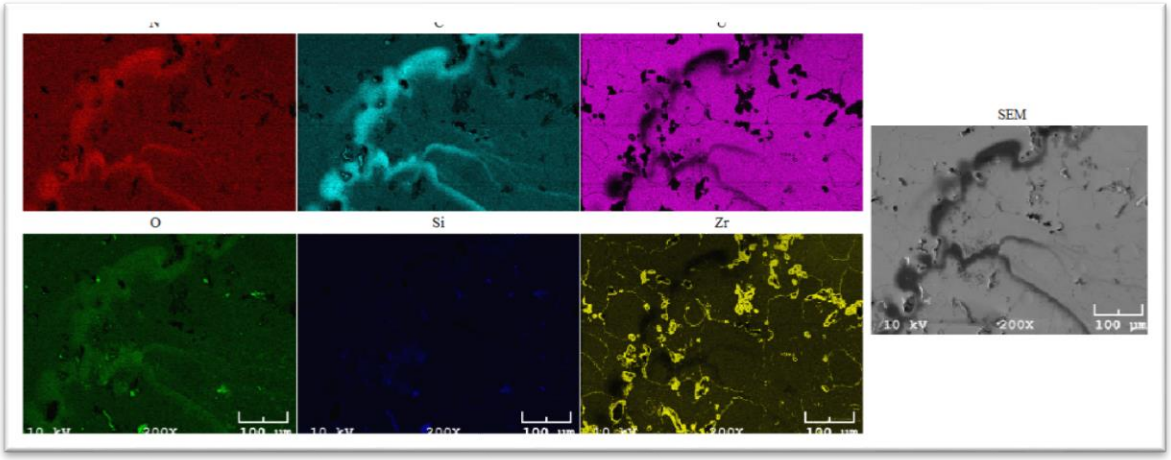

Figure 4-9: EDS map of pellet three

Figure 4-10 highlights SEM images of pellet four. The object in the bottom right of

the left image is the edge of the copper ring. The peripheral of the pellet still suffered from some minor chipping during cutting. The previously discussed "gumdrop" shape is clearly seen. However, the two regions separately are fairly homogeneous with respect to porosity and alloying. This was originally blamed on a possible temperature difference between the pellet face resting on the crucible and the exposed face, however after changing the pressing procedure with better in dye mixing the artifact disappeared. The dense interior shows larger pores however the density was larger than the other pellets measured by calipers. The zirconium rings are once again abundant. A composition map was performed but not saved for this sample.

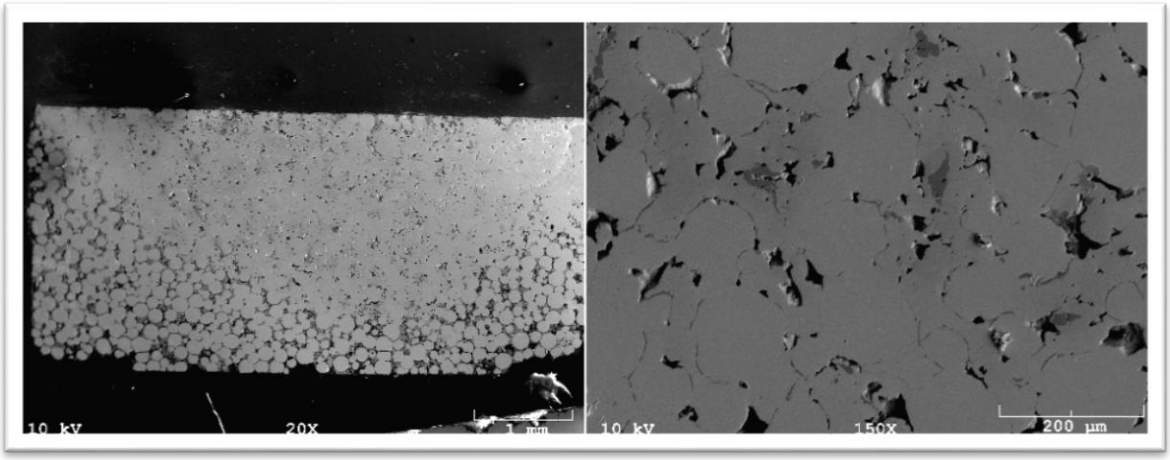

Figure 4-10: SEM images of pellet four

Stratification is almost non-existing in pellet five as shown in the top left image of Figure 4-11. Alloying and porosity is much more homogeneous than before. The top right image shows the area the composition map was performed in. The usual features

can be seen as they did in the 12 hour sintering. The composition spectrum is included to show that uranium and zirconium were dominant. A map of Nitrogen was not included since its presence on the spectrum was much less significant than in pellet three and nearly eliminated by the use of the ultra-high purity argon cover gas. This is evident in the spectrum, where nitrogen x-rays are typically found in the 0.4keV range. [29]

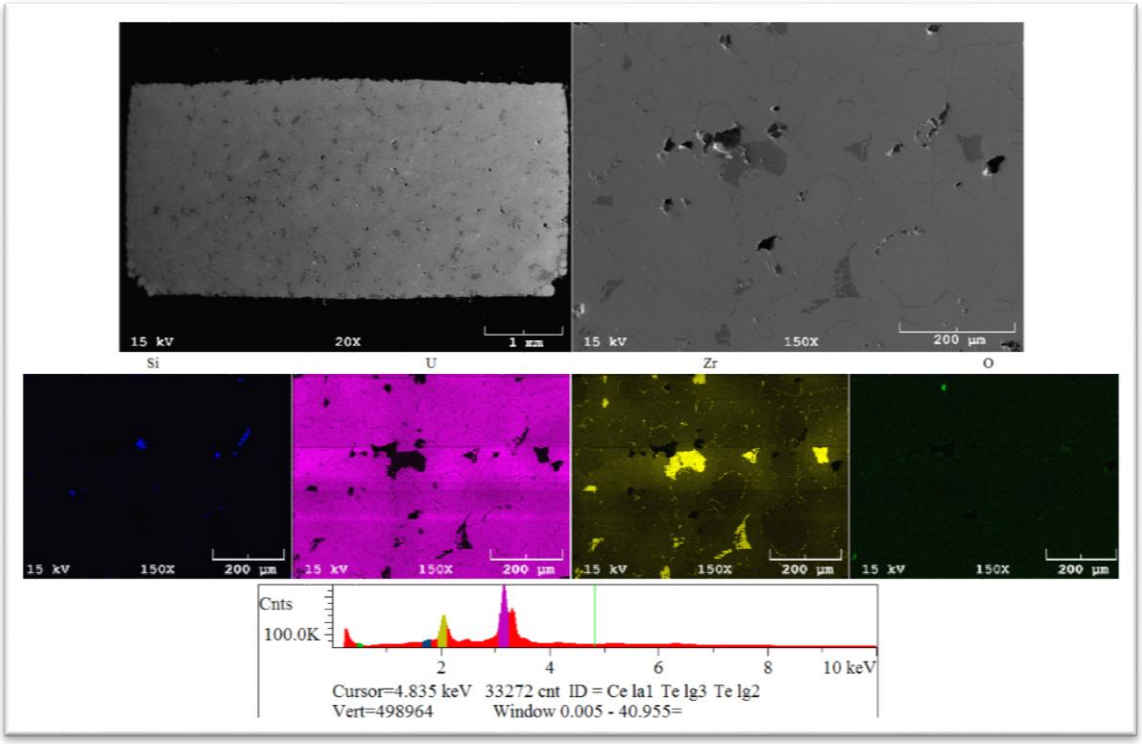

Figure 4-11: SEM imaging and EDS mapping of pellet five

Pellet six exhibited excellent homogeneity. Sintered at only eight hours, the limited diffusion of zirconium and uranium can be seen in the EDS maps of Figure 4-12 compared to pellet five. However, the zirconium rings of the previous samples have

been replaced by open pore areas surrounding what appears to be the original uranium spheres. The EDS shows increased oxygen and zirconium content in these pores.

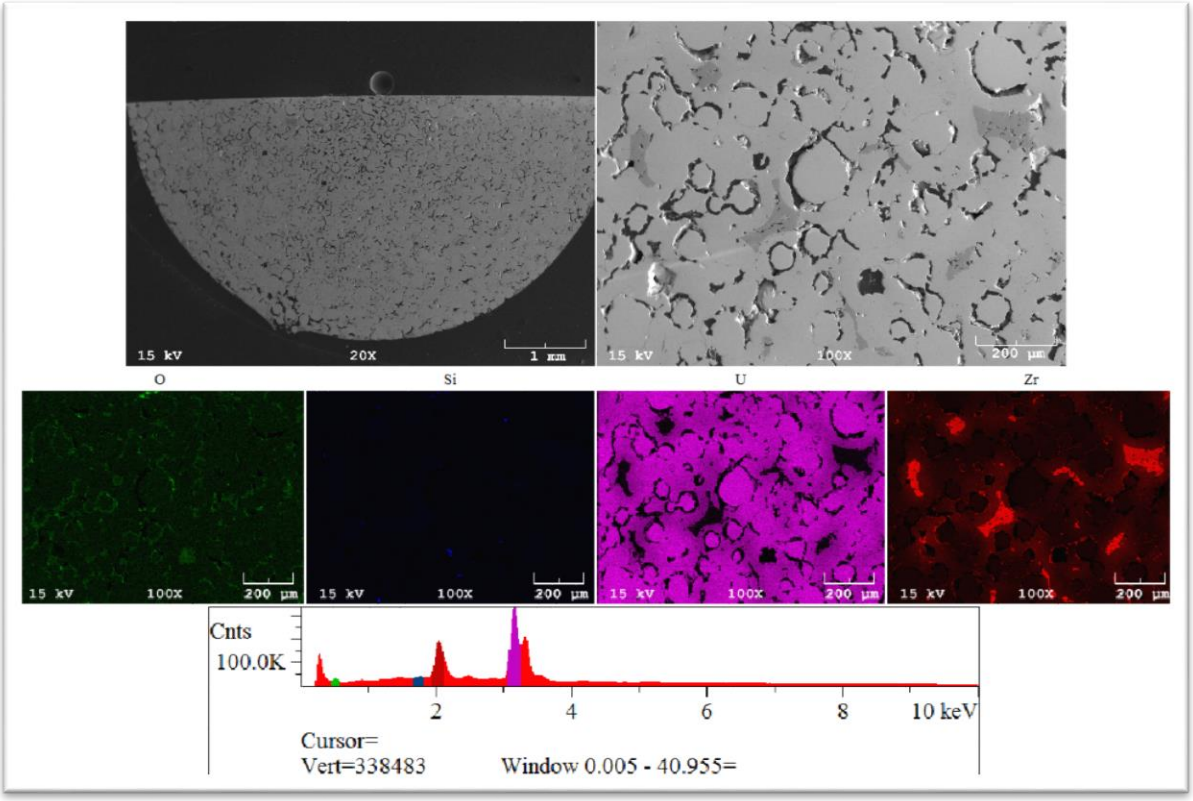

Figure 4-12: SEM imaging and EDS mapping of pellet six

In Figure 4-13, pellet seven showed diffusion of zirconium and uranium at six hours sintering. Zirconium rings exist but are very faint. A larger amount of oxygen existed in this sample than previous samples. However, there existed more and larger regions of zirconium enrichment/uranium depletion than in the longer sintering times. Additionally, porosity was extremely decentralized.

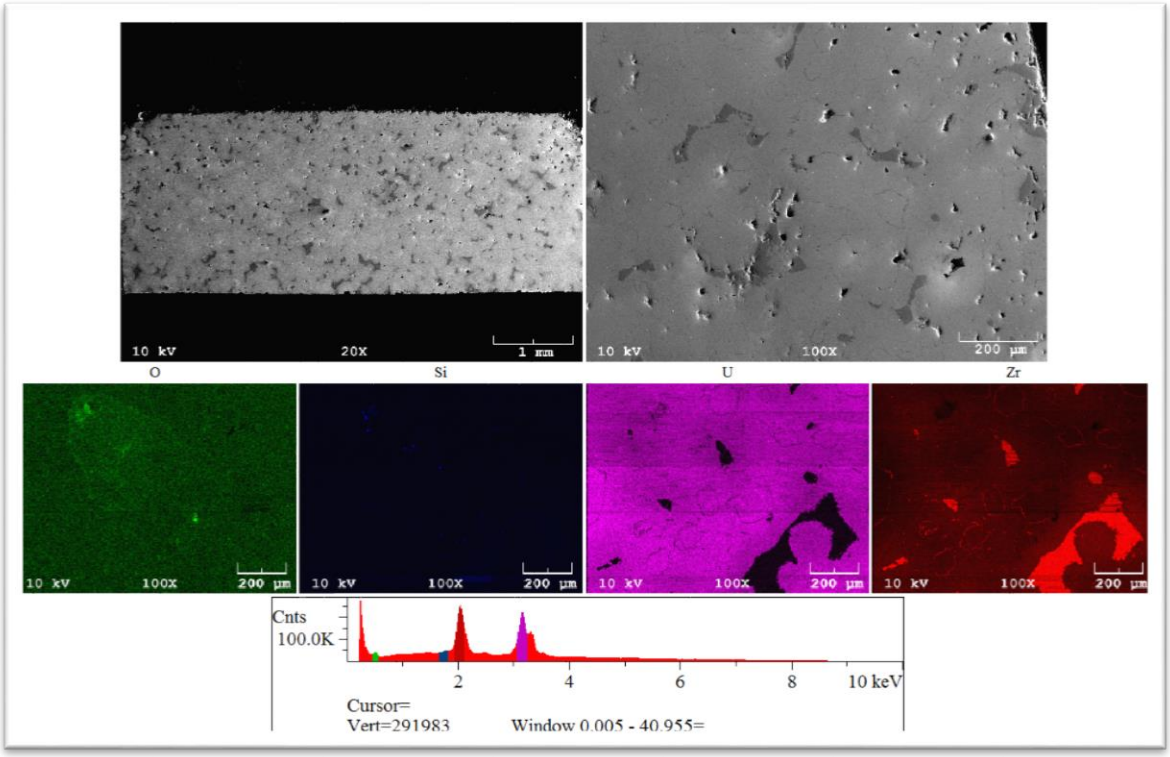

Figure 4-13: SEM imaging and EDS map of pellet seven

Pellet eight was only sintered for four hours. Despite that fact, significant diffusion can still be seen in figure 4-14. The previous zirconium rings are almost non-existent at this point. The sample was mostly homogeneous with respect to porosity with the exception of some higher density areas near the peripheral region as can be seen in the top left image.

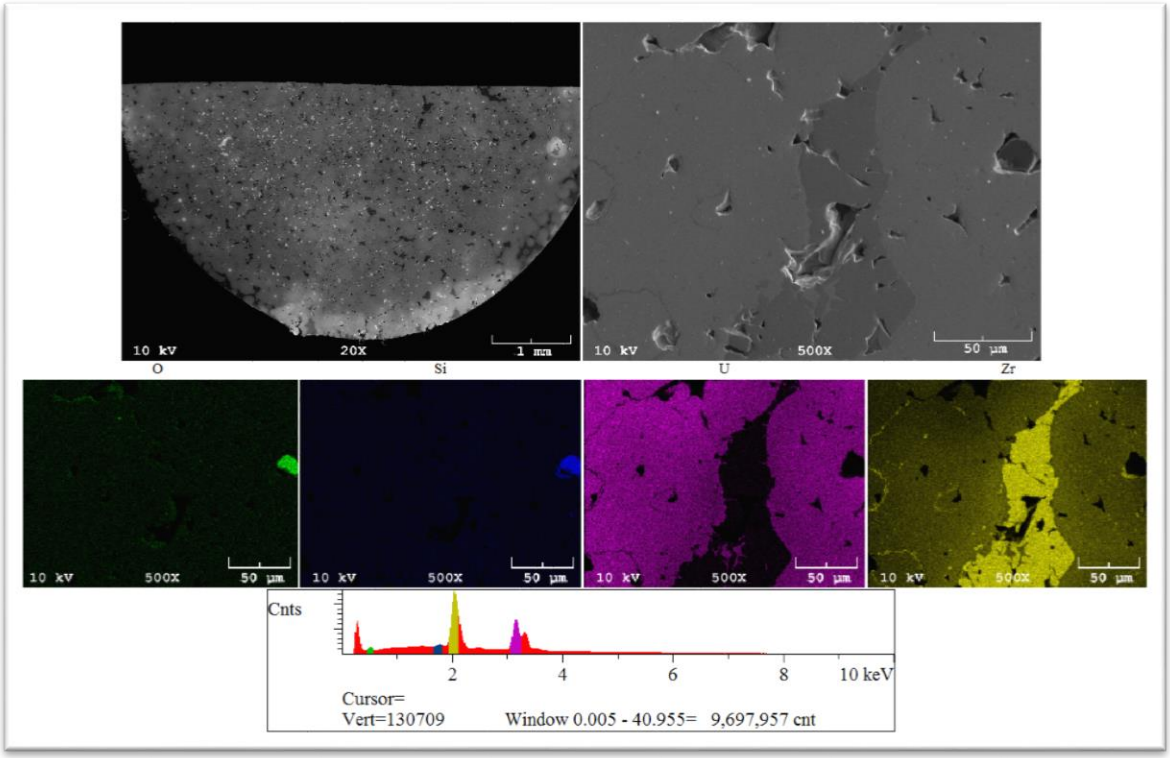

Figure 4-14: SEM imaging and EDS mapping of pellet eight

At two hours sintering, there exists a clear separation of the pressed uranium and zirconium. This is shown in figure 4-15. Hardly any sintering or alloying took place, however, despite the uranium not diffusing, small amounts of zirconium did diffuse into the uranium spheres. Some pull out did occur during polishing. Excluding pull out, porosity was fairly homogeneous. A small amount of oxygen contamination existed throughout the sample. Silicon impurities were almost non-existent since pores were small.

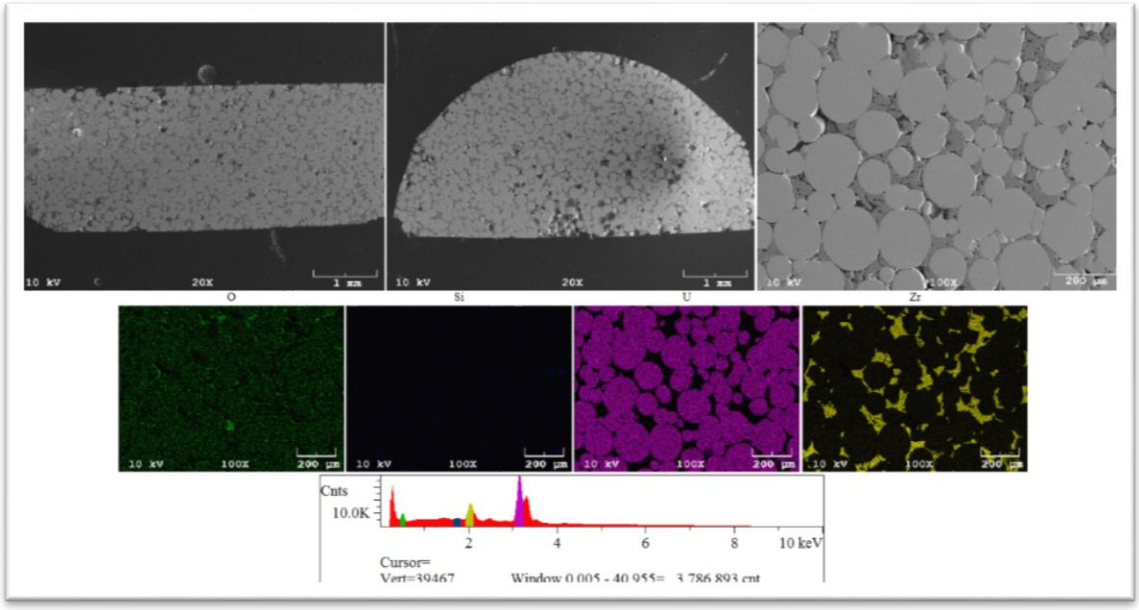

Figure 4-15: SEM imaging and EDS mapping of pellet nine

Pellet ten was sintered twelve hours to replace the results from pellet four. As can be seen in figure 4-16, pellet ten did not suffer from the uneven alloying and porosity previously experienced. Additionally, the channels of porosity returned but to a lesser extent that previously noted. Some pull out during polishing was experienced. The zirconium rings returned. The EDS composition map was used to focus solely on zirconium and uranium.

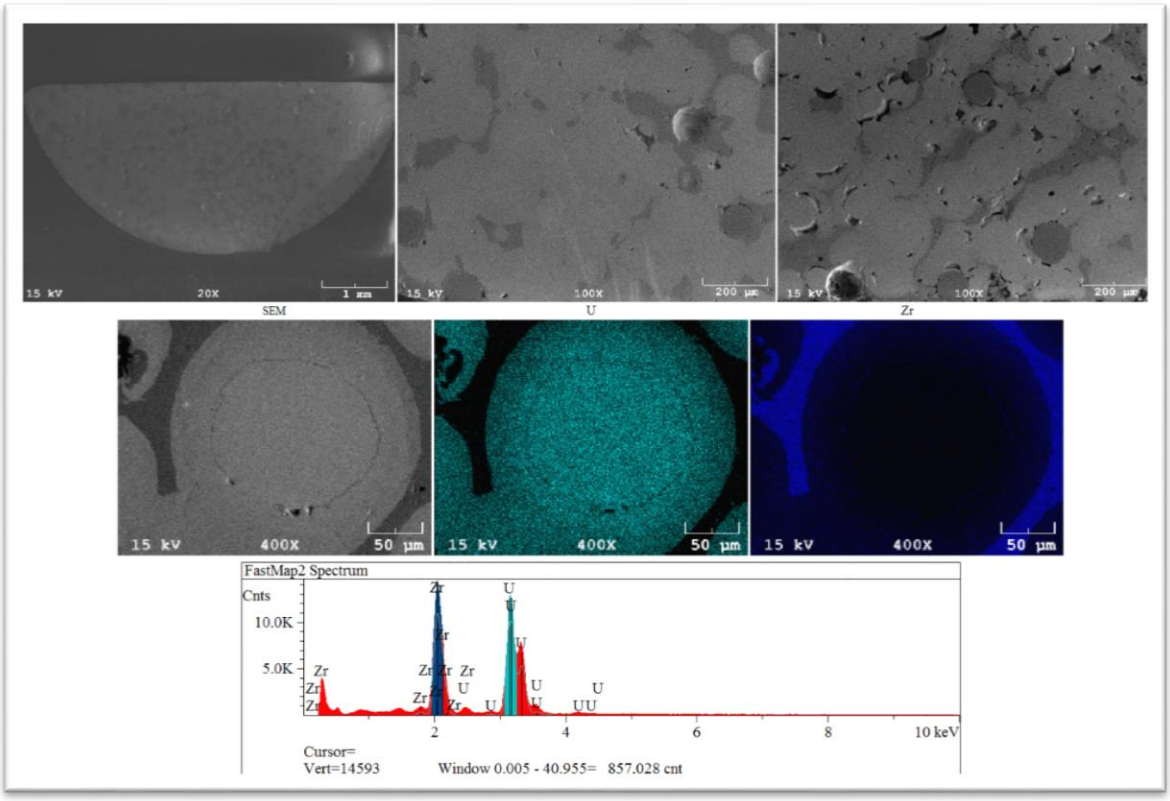

Figure 4-16: SEM images and EDS mapping of pellet ten

In Figure 4-17, a point composition map was conducted across the widest point of a single, randomly selected sphere with an obvious boundary and zirconium ring. The box, measurement 1, was an averaged composition of the area measured. Each analysis was conducted on a point across the diameter of the sphere with focus on the zirconium circle, the trend outside the circle, and the trend inside the circle. Point ten in the analysis was added to include an additional analysis directly on the zirconium ring. Table 4.3 shows the results from each analysis and figure 4-18 provides a graph for visual analysis. The thicker lines in the table denote the location of the ring. Point 10 is

excluded from the graph since it is not in-line with the others. Point 1 is outside the sphere and denotes the pure zirconium region. Zirconium has diffused all the way through this sphere. The original uranium sphere, approximately 150 microns wide, is nearly 30% by weight zirconium at the center. Additionally, the variance of zirconium within the ring is actually very limited with only an approximate 12% difference. This forms a reverse plateau in the graph. Interestingly, there are two sharp changes in concentration on the right side of the sphere near points 14 and 17 while the left side is almost uniform in concavity and somewhat uniform in slope (with the exception of point 3).

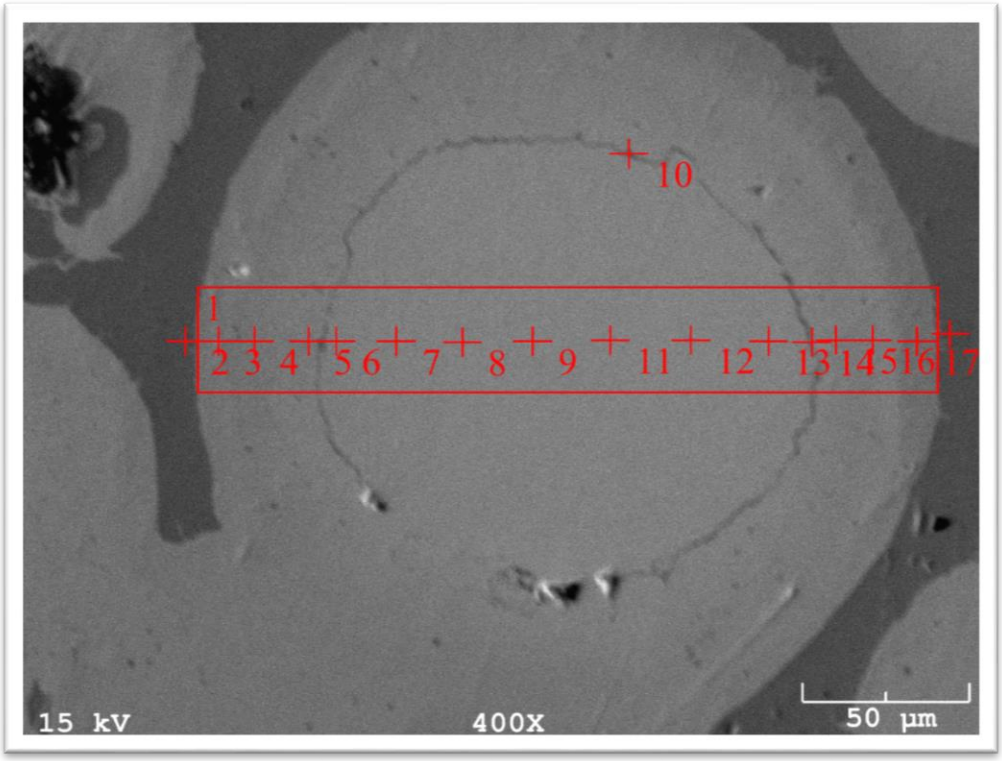

Figure 4-17: Detailed composition analysis across a representative sphere

Table 4.3: Detailed EDS analysis of a representative sphere

Meas #	Position	Dist from Centerline	Dist. from "Ring"	%Zr
	~µm	~µm	~µm	
1 (bulk)	N/A	N/A	N/A	29.6
2	0	110	35	100
3	5	105	30	77.6
4	15	95	20	69.2
5	30	80	5	51.8
6	40	70	5	42.4
7	60	50	25	34.0
8	80	30	45	32.6
9	100	10	65	29.9
11	120	10	60	30.9
12	145	35	35	32.4
13	170	60	10	39.4
14	180	70	0	45.0
15	185	75	5	61.6
16	200	90	20	71.8
17	215	105	35	83.7
18	220	110	40	100
10	N/A	85	0	89.9

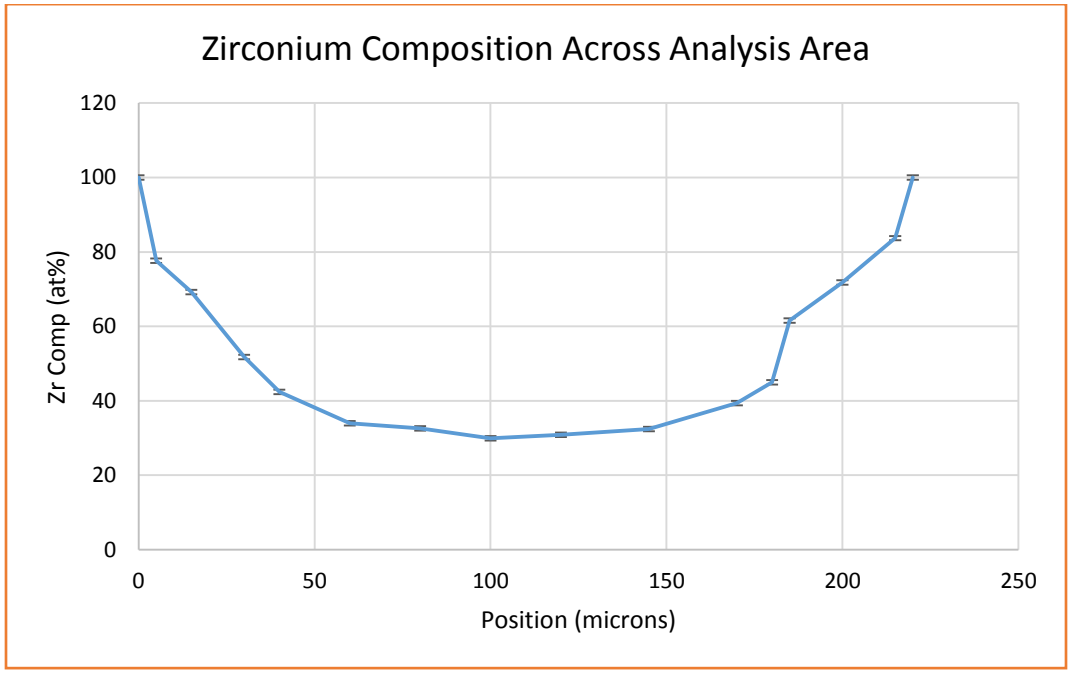

Figure 4-18: Graph of EDS detailed analysis

Table 4.4 compares the previous density measurements from above with the image analysis results. These results are from images of pellets five through ten as discussed above and arranged in order of sinter time. Percent area, circularity, and particle sizes were recorded for each parsed image and averaged. The scale was calibrated for each set of parsed images to make the particle size measurement meaningful. Immediately, a large difference in area analysis and physical measurements is noticed. This is because the error generated by the irregular surface shapes and some boundary regions were omitted during the image analysis. Even samples that appeared very porous during imaging measured over 90 percent dense. Circularity also showed a growing trend as a function of sintering with the exception at six hours sintering. Six and twelve hour

sintering shared a very similar area fraction and average particle size as well. Particle size varied as a function of area fraction more than anything else. The eight hour sintering sample exhibited a very large porosity shape because of the channels that formed as shown above. These channels also resulted in a lower circularity ratio because of the increased surface area. Additionally, the 2 hour sample had an extremely small circularity.

Table 4.4: Density comparison and image analysis results

Sinter	Area Analysis	Circularity	Avg. Particle Size
Time (hrs)	% Dense		micron
12	98.4	0.843	8.03
10	97.3	0.754	43.6
8	91.5	0.367	124
6	98.2	0.868	9.23
4	95.7	0.651	17.9
2	96.9	5.65E-4	13.4

5. DISCUSSION

5.1 *Pressing Results*

There were five attempts to press the pellets before the first successful pellet was achieved. The fourth and fifth attempts crumbled while attempting to measure the green pellet with calipers. Because of this, the first recorded sample was not measured for its green density in an attempt to produce the first sintered pellet. All subsequent green pellets were measured although some continuing to break apart. The first pellets suffered from a severe stratification of density and alloying. The stirring rod discussed in section 3.2 was used to alleviate this and utilized after the first successful pellet. Stratification of density continued until pellet four, in which the stirring rod was used to both mix in the dye and tap the outside of the dye while pressing. The source uranium powder was also changed and new powder was generated. Additionally, pressure was pumped up in slower strokes on the carver press to prevent sticking and allow slight relaxing of the spheres between pressure increases up to rated pressure. Reducing the total mass of powder used also helped reduce stratification.

Lots of care had to be taken after pressing to measure. Many pellets were still very delicate around the edges. Several pellet attempts were scrapped because the pellets split when snugging the calipers up (usually when measuring height). This caused measurement error because the calipers had to be handled very delicately and all this manipulation occurred through glove box gloves which greatly reduced dexterity.

The use of the split dye also caused slight errors in volume measurements. As seen in

Figure 5-1, the split sections caused slight bumps along the radius highlighted with yellow circles. This skewed the volume measurements making the density appear lower than it actually was.

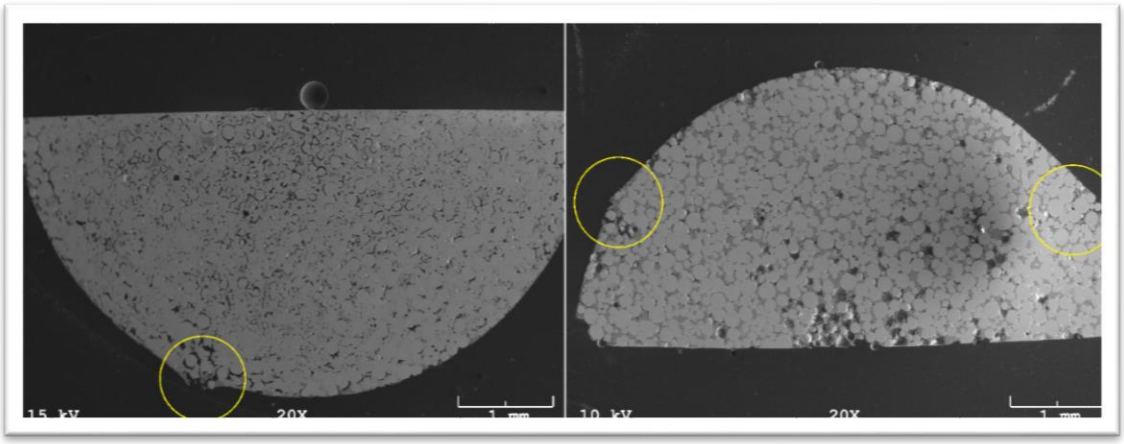

Figure 5-1: Swollen areas caused by the split dye

5.2 *Sintering Results*

Sintering proved more complex than originally expected. With the use of the glove box, no contamination was expected at the beginning of the experiment. However, even slight increases in the glove box oxygen levels proved to affect results. Pellet one is shown in figure 5-2 shortly after sintering was complete. Oxygen levels in the glove box reached only 5 ppm, however oxygen trapped in the insulation used to make the heater rig was sufficient to discolor the sample radically. Due to this, the heater was off-gassed by running it at 1000 degrees Celsius for 24 hours after this run.

Figure 5-2: Browning and blackening of pellet one due to oxygen during sintering

Pellet three came out with a golden/yellow color. This was caused by the nitrogen in the glove box as discovered in the SEM's EDS measurements. Since nitrogen isn't measured in the glove box, the exact amount was unknown. However, this required the use of a cover gas, even inside an inert atmosphere, in order to ensure atmospheric quality. Following the installation of the ultra-high purity argon cover gas, discoloration of sintered pellets was usually limited to the extreme edges and minimal.

The primary indication of sintering progress was densification. However, this wasn't as obvious as originally thought. As table 5-1 shows, the dynamics of this system were a bit more complex than a single element pellet. Small changes in mass were caused by minor losses or chips near the peripheral area. This was usually indicated by small amount of powder found loose in the crucible or in boats used to transport the sample.

Mass was expect to remain mostly constant with some minor losses during powder pouring and pellet measuring. Volume, however, was expected to decrease to indicate densification. In most cases this occurred but much more trivially than originally expected. Some even appear to have relaxed even after 12 hours of sintering. Because of this, raw trends in density appear as if no sintered had occurred. This is why some comparison to theoretical density must occur.

Table 5.1: Trends in densification

Sample	Mass_g	Mass_s	Trend	Vol_gr	Vol_snt	Trend	Dens_g	Dens_s	Trend
	g	g		cc	cc		g/cc	g/cc	
1	1.86	1.85	-0.01	*	0.133	N/A	*	13.92	N/A
2	1.72	*	N/A	0.109	*	N/A	15.71	*	N/A
3	1.02	*	N/A	0.083	*	N/A	12.30	*	N/A
4	1.10	1.08	-0.02	0.072	0.079	0.007	15.32	13.67	-1.63
5	1.13	1.13	0.00	0.086	0.085	-0.002	12.96	13.27	0.31
6	0.98	0.98	-0.01	0.073	0.072	-0.001	13.39	13.48	0.09
7	0.75	0.75	0.00	0.069	0.066	-0.003	10.90	11.38	0.48
8	0.82	0.81	-0.01	0.069	0.068	-0.001	11.90	12.04	0.14
9	0.96	0.95	-0.01	0.064	0.068	0.004	15.02	14.10	-0.92
10	0.92	0.92	0.00	0.073	0.072	-0.001	12.67	12.82	0.15

*sample not taken

Using Mash and Disselhorst's equation for penetration depth as defined in Chapter 2, Table 5.2 shows the calculated expected penetration depth of zirconium in uranium at the sintering temperature, 900°C. These depths can be utilized to define phase boundaries of the mixture and better estimate density.

Table 5.2: Time dependent penetration depth of diffusion between U and Zr at 900°C

Time	Penetration depth
2	7.96
4	11.25
6	13.78
8	15.91
10	17.79
12	19.49

Using the microsphere distribution of DU in the RES provided by Daniel Galicki [9] as shown in Table 5.3, the mean particle size can be estimated as 122 microns with a corresponding radius of 61 microns. This provides a representative uranium sphere size to estimate bulk density.

Table 5.3: Analysis of particle distribution in the RES

Particle size	Bin mean	Weight	Bin mean x	
(micron)	(micron)	(grams)		(micron)
180-155	168	5.95	996	44.7
154-125	140	3.90	544	24.4
124-106	115	4.78	550	24.7
105-90	97.5	2.85	278	12.5
89-75	82.0	2.81	230	10.3
74-63	68.5	1.15	78.8	3.54
62-53	57.5	0.453	26.0	1.17
52-45	48.5	0.252	12.2	0.549
44-0	22.0	0.139	3.06	0.137
		22.28		122

In order for the phases to be taken into account, the density of the material as a function of varying zirconium in uranium must be used. A graph of this is provided in Figure 5-2. The graph shows three regions corresponding to the regions of the phase diagram shown in Figure 5-3. The region on the left is the orthorhombic uranium and UZr_2 phase and therefore the density is a simple density of mixtures calculation as demonstrated by equation 5-1.

$$\rho_{mix} = \rho_a \times x_a + \rho_b \times x_b \quad \text{5-1}$$

where ρ is density in g/cc, x is the mass fraction, and a and b are the corresponding elements uranium and zirconium. This first region's density varies linearly from 19.1 g/cc (pure uranium) [10] to 10.3 g/cc (pure UZr_2) [11]. The middle region is a "pure alloy", where hexagonal UZr_2 is stable and constitutes the structure with no stable secondary phase. Therefore, this region is flat in regards to density. The final region is another mixture. This time UZr_2 and Hexagonal Close Packed (HCP) zirconium constitute the two stable phases. This region varies linearly from 10.3 g/cc to 6.5 g/cc (pure zirconium) [12].

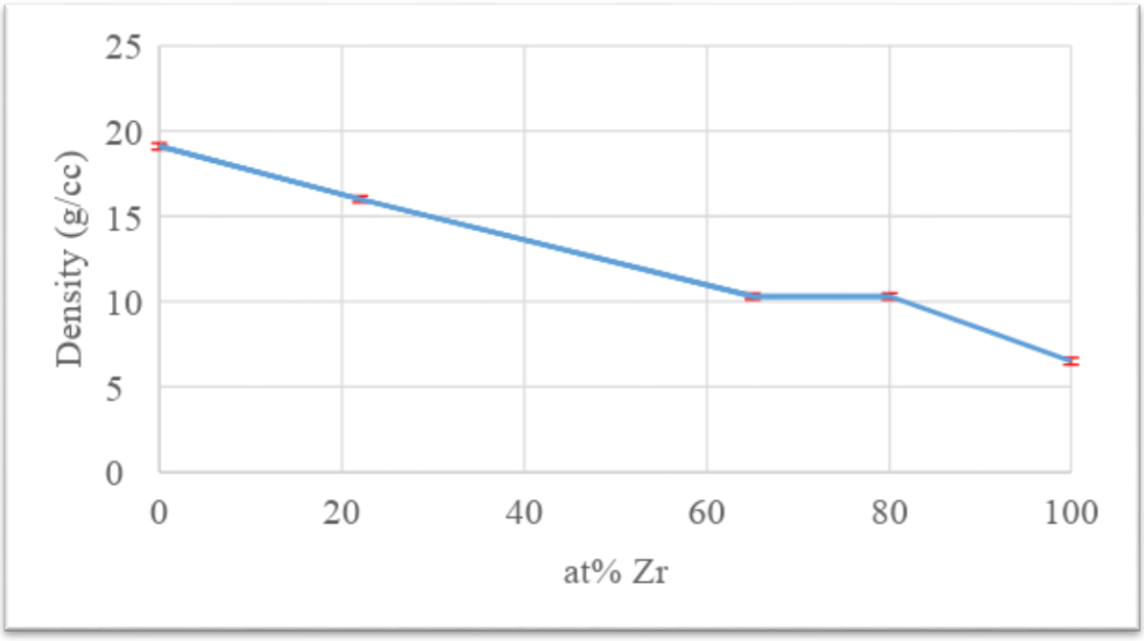

Figure 5-3: Density of the U-Zr system as a function of atomic percent zirconium at 0°C.

A model of two perfect spheres in an infinite "sea" of opposing material can be utilized to simulate diffusion as shown in Figure 5-4. These spheres represent an idealistic, single average sphere in the pellet. If a thin sliver passing through the center of the sphere is analyzed, it appears as a diffusion couple with diffusing material on both sides of the focus material. For the uranium which experiences only minor shape distortion under pressing, this is an accurate model to the real world application. For the zirconium, this is a very rough estimate since it is distorted after pressing.

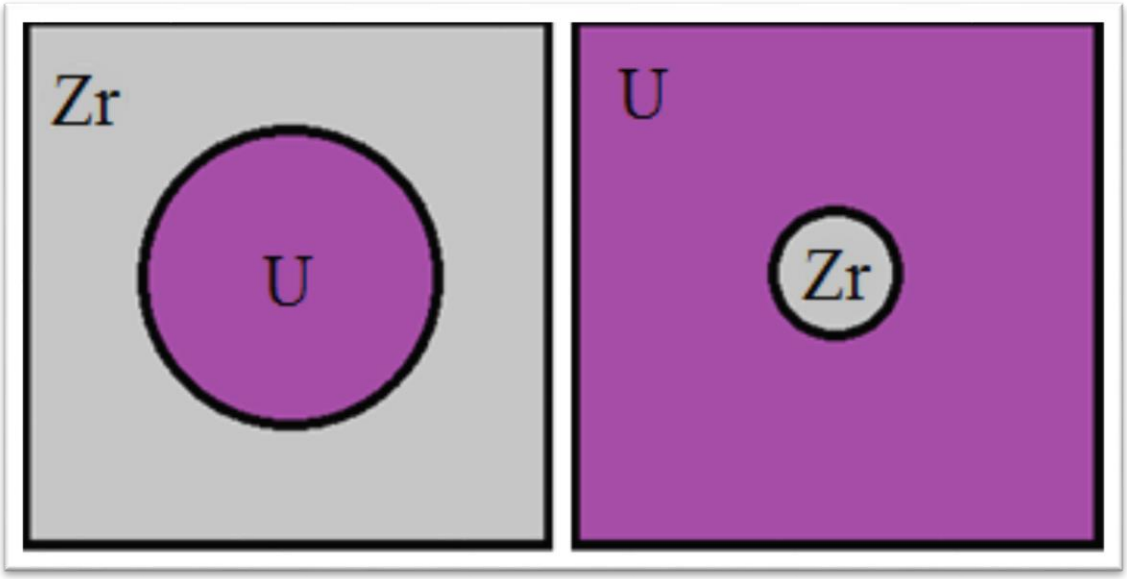

Figure 5-4: Model of an ideal system for diffusion calculations.

Diffusion boundary layers are necessary to identify density zones. Since there are no controlled boundaries, it is necessary to make some assumptions. Assuming that the diffusion boundary exists at the exterior of the individual sphere and, despite real diffusion mechanics, it remains at this point throughout the entire sintering evolution, this peripheral point can act as an anchor for subsequent equations. This assumption comes with errors, especially since once one material fully penetrates the other that the diffusion rate changes and the diffusion barrier shifts. Now, moving into the uranium sphere, the peripheral is designated as the 50 atom percent zirconium reference (the diffusion barrier). Therefore, within the uranium microsphere, only two zones exist based on the phase diagram: 1) the pure uranium zone, untouched by zirconium diffusion and 2) a zone of a mixture of pure uranium and UZr_2. The zirconium

microsphere becomes a bit more complex, as four zones exist: 1) the pure zirconium center, 2) the zirconium and UZr_2 mixture, 3) the stable UZr_2 phase, and finally 4) the remaining uranium and UZr_2 mixture. A graphical representation of these boundaries are shown in Figure 5-5 along with the representative equations to define those boundaries. The 61 and 22 microns in the equations are the corresponding sphere radii.

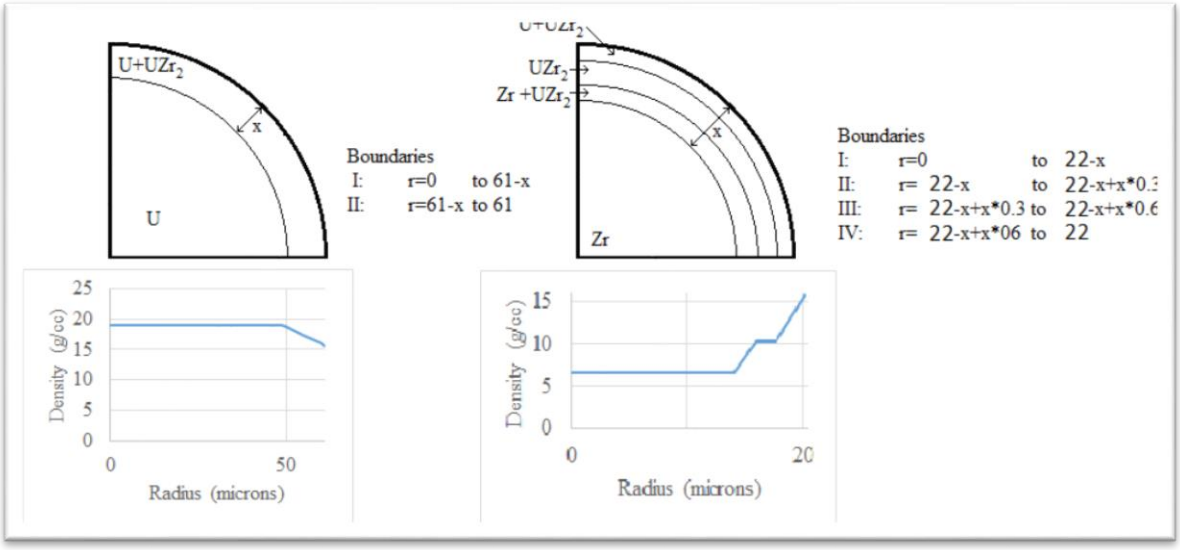

Figure 5-5: A graphic representation of phase boundaries and their corresponding densities using x=12 microns.

Now, assuming the atom percent variation is linear through the penetration depth and that an infinite amount of material is available for diffusion outside the spheres, a theoretical density for the pellet can be estimated. These assumptions simplify the equations and allow for the focus to be on the diffusion into the spheres. Therefore, the theoretical density for the uranium sphere is found using equation 5-2.

$$\rho_{TD_U} = 19.1\frac{g}{cc} \times \frac{(61-x)^3}{61^3} + 15.7\frac{g}{cc} \times \frac{(61)^3-(61-x)^3}{61^3} \quad 5\text{-}2$$

where ρ_{TD_U} is the total theoretical density for the uranium sphere in g/cc when accounting only zirconium diffusion into uranium, x is the penetration depth found by equation 2-1, 61 microns is the average sphere radius calculated above, 19.1 g/cc is the theoretical density of alpha uranium as mentioned above, 15.7 g/cc is the average theoretical density of the alpha uranium and UZr_2 phase mixture found between 0 and 50 at% Zr. Since the outside face of the uranium sphere is used as the diffusion boundary, this calculation only covers 0 to 50 atomic percent zirconium. Plugging in the values for 12 hours of sintering, the theoretic density becomes 17.47 g/cc. While this is within the expected 17.84 to 16.02 g/cc bounds for the alloy, ignoring the zirconium volume creates an error. This is evidenced by plugging in a diffusion length of zero which would return pure uranium density.

If the result from above were simply plugged into the density of mixtures equation, the result would be 16.38 g/cc. This is still within the bounds of our expected system density, however, at maximum diffusion into the uranium (x=61 microns), the result is considerably less than the 16.02 g/cc bound (14.78 g/cc). This accuracy is improved by calculating the zirconium density changes with the simulated microsphere. This can be handled with the same method as uranium. By using the same system of bounds and volumetric fractions of density shown in fig. 5-4, only converted to the zirconium side of the U-Zr phase diagram, equation 5-3 can be derived:

$$\rho_{TD_{Zr}} = 6.5\frac{g}{cc} \times \frac{(40.4-x)^3}{40.4^3} + 8.4\frac{g}{cc} \times \frac{(22-0.4x)^3-(22-0.7x)^3}{22^3} + 10.3\frac{g}{cc} \times$$

$$\frac{(22-0.4x)^3-(22-0.7x)^3}{22^3} + 11.32\frac{g}{cc} \times \frac{(22)^3-(22-0.4x)^3}{22^3} \quad 5\text{-}3$$

Where $\rho_{TD_{Zr}}$ is the total theoretical density for the mixture in g/cc when accounting only uranium diffusion into zirconium, x is the penetration depth found in eqn. 2-1 in microns, 40.4 microns is the effective sphere radius for the zirconium calculated above, 6.5 g/cc is the theoretical density of HCP zirconium, 8.4 g/cc is the average theoretical density of the HCP zirconium and UZr_2 phase mixture found between 80 and 100 atomic percent zirconium, 10.3 g/cc is the theoretical density of the UZr_2 phase, and 11.32 g/cc is the average theoretical density of the alpha uranium and UZr_2 phase mixture found between 65 and 50 atomic percent zirconium. Using the same diffusion length as above, this equation returns a value of 9.01 g/cc. When the density of mixtures equation is applied, the final estimated theoretical density is 16.62 g/cc. Checking the equation bounds for x, the values of 17.84 and 16.04 g/cc are generated.

The morphology of zirconium when pressed with uranium is heavily dependent on the pressing procedure, the type of equipment used, and the starting zirconium sphere size. In real pellets, zirconium distributions are very sporadic in size, spacing, and homogeneity.

Plugging in the values from Table 5.2, Table 5.4 contains the corresponding theoretical densities for the respective sintering times used. The resulting trend is shown in Figure 5-6.

Table 5.4: Time dependent penetration depth of diffusion between U and Zr at 900°C and the corresponding theoretical densities

Time (hrs)	Penetration depth (microns)	Theoretical Density (g/cc)
2	7.96	17.01
4	11.25	16.73
6	13.78	16.53
8	15.91	16.37
10	17.79	16.25
12	19.49	16.14

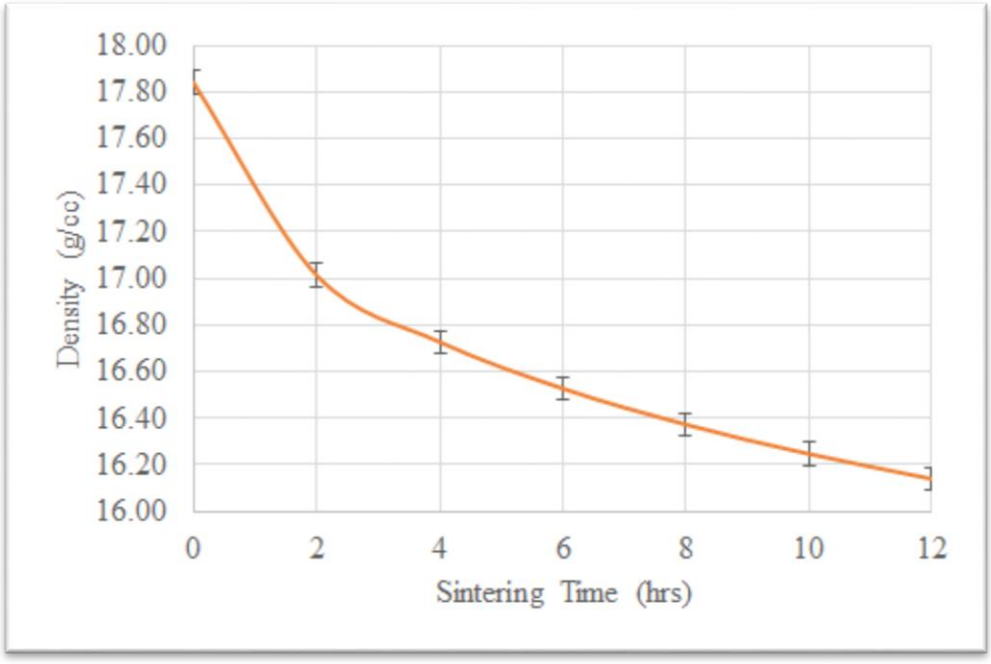

Figure 5-6: Theoretical density trend as calculated from 0 to 12 hours at 900C.

When taking in account theoretical density, including the calculated form, the results

make more sense. This is caused by the change in structure from the single element uranium and zirconium system to the full spectrum of the uranium-zirconium phases. Table 5.5 shows the trends with percent theoretical density. It is arranged by sample number, top, and sintering time, bottom. Sample four is omitted in the second set because it is an outlier. With the exception of sample four, which suffered from nitrogen contamination and stratification, all samples performed as expected. The trend shows relaxation at two hours centering and densification quickly after. Minor variations in the amount of densification can be explained by individual flaws or contaminants in each pellet. For instance, sample sixes increased porosity channels, likely caused by oxygen contamination on the uranium spheres before centering, caused a drop in density and a minor bump in the trend.

Table 5.5: Trends in theoretical density

Sample	% TD_gr	%TD_sntr	Trend	Hours sintered
4	85.76	84.73	-1.04	12
5	72.65	81.68	9.03	10
6	75.06	82.33	7.28	8
7	61.10	68.82	7.73	6
8	66.70	71.95	5.24	4
9	84.19	82.89	-1.31	2
10	71.01	79.43	8.42	12
Hours sintered	% TD_gr	%TD_sntr	Trend	Sample
12	71.01	79.43	8.42	10
10	72.65	81.68	9.03	5
8	75.06	82.33	7.28	6
6	61.10	68.82	7.73	7
4	66.70	71.95	5.24	8
2	84.19	82.89	-1.31	9

5.3 *Image Analysis Results*

Because of delamination, excessive damage during processing, and stratification, the first four samples results were discarded for final analysis. Pellet four, originally intended to be used, failed to fully densify and therefore had to be replaced by the final sample. These served primarily as lessons learned in the process refining phase and are less important than the finalized results.

Beginning with the shortest sinter time, pellet nine was held at soak temperature for two hours. The density trend, both actual and percent theoretical, shows relaxation of the pellets at this sintering stage. Figure 4-15 clearly showed irregular porosity shapes and a lack of diffusion. Taking a closer look with figure 5-7, we can see that while uranium didn't diffuse hardly at all, zirconium had already begun penetrating into the uranium spheres. A small amount of error was expected between area analysis and measured densities, however a 14.0% increase was observed. The errors during measurement are likely a culmination of the problems discussed in the previous section and the fact that area fraction is an estimate at approximately the centerlines of the pellet. This means porosity and deformation on the extremes of the pellet were ignored in image analysis. The circularity measurements were extremely small. This is because pores had not begun to conglomerate yet and still appeared "as pressed". The elongated channels and rough shapes means particles had a large perimeter to area ratio and therefore a very small circularity. Finally, particle size began at an average 13.4 microns. Since zirconium particles began at 44 microns and deformed during pressing, this is expected.

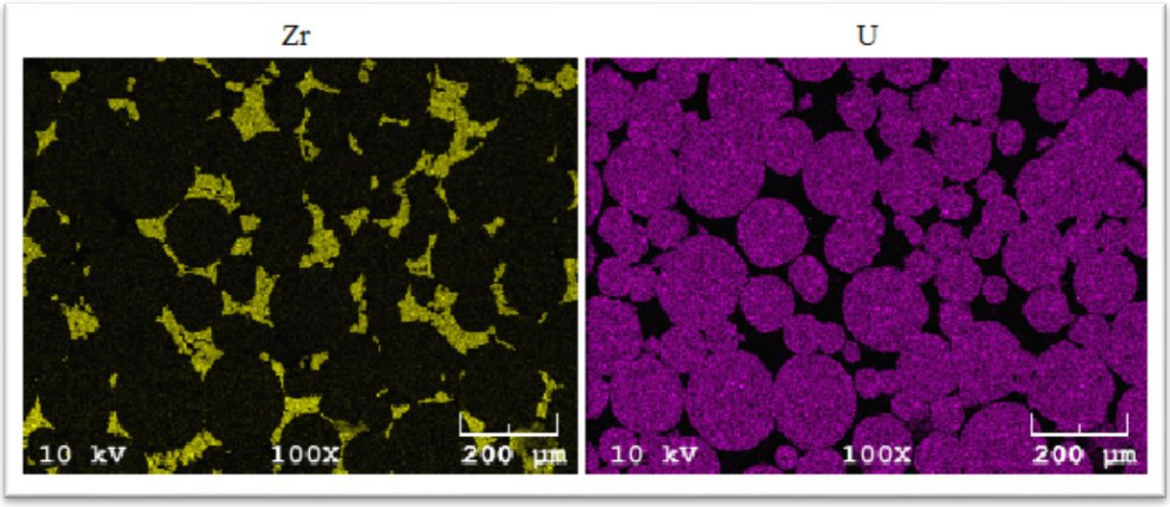

Figure 5-7: Close-up of diffusion at two hour sintering

After only four hours of sintering, significant diffusion was evident in the EDS maps. Zirconium had diffused through most of the sample while uranium had shown some penetration into the zirconium rich areas as well. Areas of pure zirconium still existed in large sections. This was the first sample exhibiting the formation of the zirconium rings. They were very faint and mostly evident on EDS imaging. Since zirconium has a lower Gibbs free energy of formation with oxygen than uranium, zirconium was scavenging oxygen to form zirconium oxide. The most likely oxygen contamination is on the outside of the spheres. Since zirconium deformed during pressing, that would leave most of the oxygen concentrated on the outside of the uranium spheres with some minor areas where the outside radius of the zirconium spheres might have become pinched or trapped without contacting uranium. This also explains why zirconium diffused through this oxide layer readily. Zirconium was pulled into the layer and uranium would have

had to overcome the layer to diffuse further. Since oxides of uranium and zirconium diffuse at different rates, this is also a point of error in the equation for theoretical density and the diffusion model utilized. Additionally, this sample had a slightly more diffused peripheral area than internal, The only final pellet to exhibit this slight stratification, it shows that a slight temperature gradient might exist from the center of the pellet to the outside, despite the slow ramp rate utilized. The area fraction once again deviated from the physical measurements. This time the error was 23.8% difference. Circularity increased vastly. Unlike the previous sample, porosity had moved into the uranium enriched areas and coalesced. In Figure 5-8, the evolution of porosity can be seen between the sintering times of two to four hours. Both images were taken at 100 time magnification, cropped, unedited, and not resized. The contrast was set slightly different between the images during imaging. The darker area in the left picture is pure zirconium, similar to the dark area on the left side of the right image. Pore size grew as the joined and diffused. This explains the increased average pore size from 13.4 to 17.9 microns.

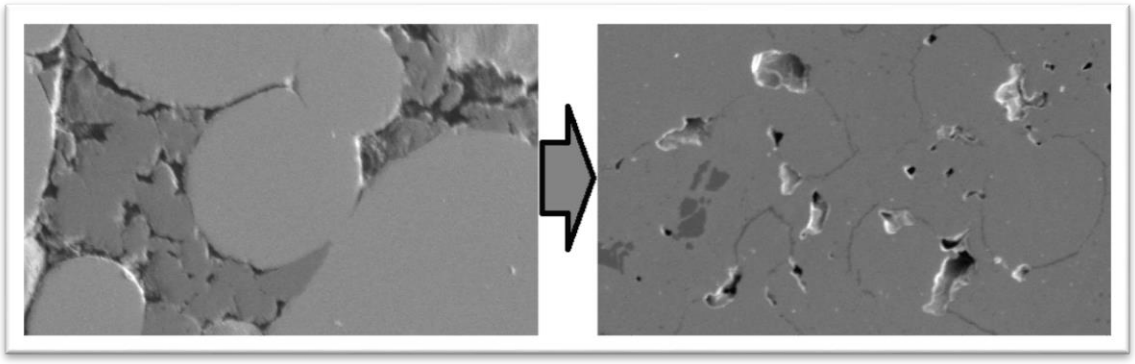

Figure 5-8: Evolution of porosity from two to four hours of sintering

After six hours of sintering, porosity and sintering appeared extremely homogeneous. Zirconium appear throughout the sample with very few enriched areas. Uranium had diffused in such a manner that it was difficult to pinpoint the original uranium-zirconium interfaces. Also, porosity had diffused thoroughly into all regions. Zirconium rings were more developed after this sintering period and more closed into full rings. Figure 5-8 shows this evolution and changes in topical morphology in this step. These images were only cropped and both were taken at 100 times magnification. At almost 30% difference, the area fraction error is largest in this sample. This sample had the largest average circularity. Examining Figure 5-9, it is not difficult to see why. Most pores had taken an oval to trapezoidal shape in this step. Finally, the average pore size had decreased in this step despite pores previously conglomerating. This is because the same volume of pores are now taking up a smaller surface area since they are closer to spherical, which also explains the large difference between area fraction and measured density.

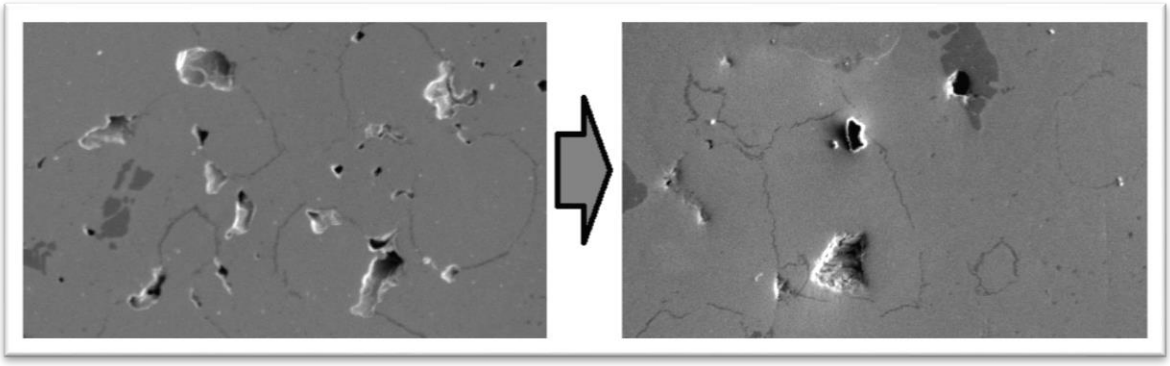

Figure 5-9: Evolution of porosity from four to six hours

At eight hours, pellet six had formed channels of porosity. An interesting phenomenon, uranium had more thoroughly diffused in this sample than zirconium. The channel formation seemingly limited zirconium diffusion but uranium diffusion appears to have "leaped" over the channels. In fig. 4-12 above, zirconium followed routes around the pores while uranium diffused isometrically despite the channels. The EDS map shows a slight increase in oxygen, especially in some of the channels. Because of the limited zirconium diffusion, more and larger zirconium rich zones exist in this sample than the previous. The zirconium rings have apparently disappeared, being replaced with these channels. These channels reflected a considerable drop in density as measured by area fraction. At less than ten percent difference, it is the closest to the physical measurements. The circularity measurement also decreased considerably due to the increased perimeter of pores. Finally, pore size increased immensely due to the elongated, continuous shape of the pores.

At ten hours, the pellet looked extremely solid from center to edges. Zirconium had diffused into almost the entire volume of the pellet. Very few zirconium rich/uranium depleted regions remained. Once again, zirconium rings appeared throughout the sample. Similar to the six hour sample, pores were dispersed and fairly circular. The area fraction difference was 15.6% compared to sintered measurements. Circularity increased to around the same as when sintered for six hours. However, pore size still showed a marked increase. Additionally, many pores hugged the zirconium rings in the sample as shown in Figure 5-10. The figure highlights the spheres porosity is centered on in random locations of this sample. Each image is at 75 times magnification and unedited except for cropping. This trend appears to correlate with the channels formed at the eight hour mark. Here, they are reabsorbed into the structure and are beginning to distribute outward from these channel regions.

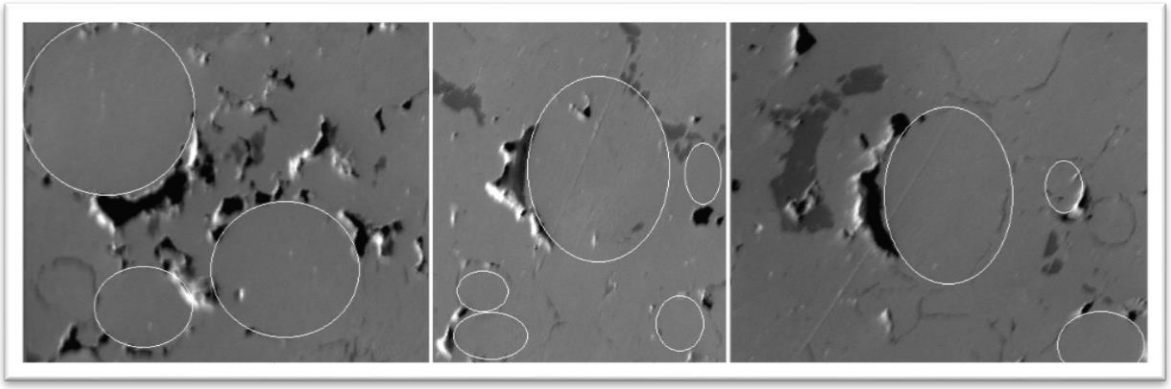

Figure 5-10: Highlight of spheres pores are centered on.

Twelve hours of sintering produced a very solid pellet with little stratification. Some areas near the peripheral had slightly higher porosity than in the center. Zirconium and uranium diffusion looked about the same as at ten hours sintering. Zirconium rings and pore channels still existed in this sample, however the channels were much thinner and existed mainly near the top and bottom surfaces of the pellet (the circular faces of the cylinder). Figure 5-11 shows an evolution of these channels with representations from each pellet from six to twelve hours sintering. It should be noted that these are not the same spheres or pellets. A similar shape and sized microsphere and pore were found from each sample. Not many of these spheres with adjacent porosity existed at six hours.

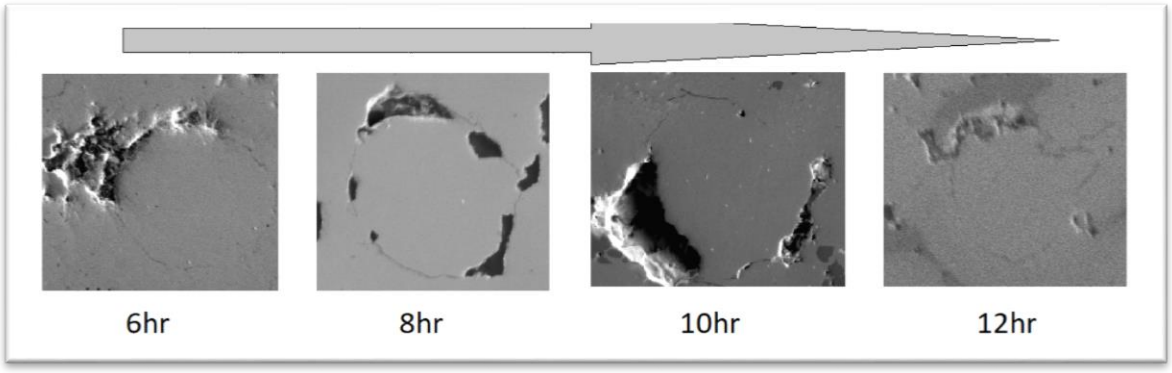

Figure 5-11: Evolution of porosity at pore boundaries.

Once again, at six hours, the majority was found at the extreme top and bottom of the pellet, while in the eight and ten hour samples they are found throughout. The area fraction average proved to be the highest in this sample. The fraction was 19 percent

above the measurement but much more believable with the images captured. Circularity increased as more of the channels disappeared. Pore size also dropped sharply back to about what it was at six hours sintering. Much smaller pores appeared near the rings and any remaining channels were very shallow and partially formed as can be seen in the right image of fig. 5-11.

As discussed in the previous chapter, a point composition analysis was conducted on a single, representative sphere. Interestingly, the area average conducted in the rectangle had a lower zirconium composition than the lowest point on the line measured. In the visual image, not much zirconium appears to exist on the interior of the zirconium ring. The average provided for the region was 29.6 atomic percent zirconium or 13.9 percent by weight. The lowest point evaluated was at 29.9 atomic percent. The range inside the zirconium ring was 29.9 near the center to 42.4 at% near the ring. The ring itself, measured in two locations, returned 45 and 89.9 at%. Two locations just outside the sphere were also recorded and 100% zirconium was observed. The distance from the centroid of the zirconium ring, the center of the original uranium sphere, to the zirconium ring is 70 microns. The distance from the zirconium ring to the pure zirconium region is 35 microns. The calculated diffusion length for twelve hours was only 19.5 microns. For zirconium, this seems to be a poor representation. For uranium outward diffusion, the estimation is approximate and the disparity might be explained by diffusion through the oxide layer. The estimate provides a standing point to compare the results and make sense of the numbers. Any error is systematic.

6. SUMMARY AND FUTURE WORK

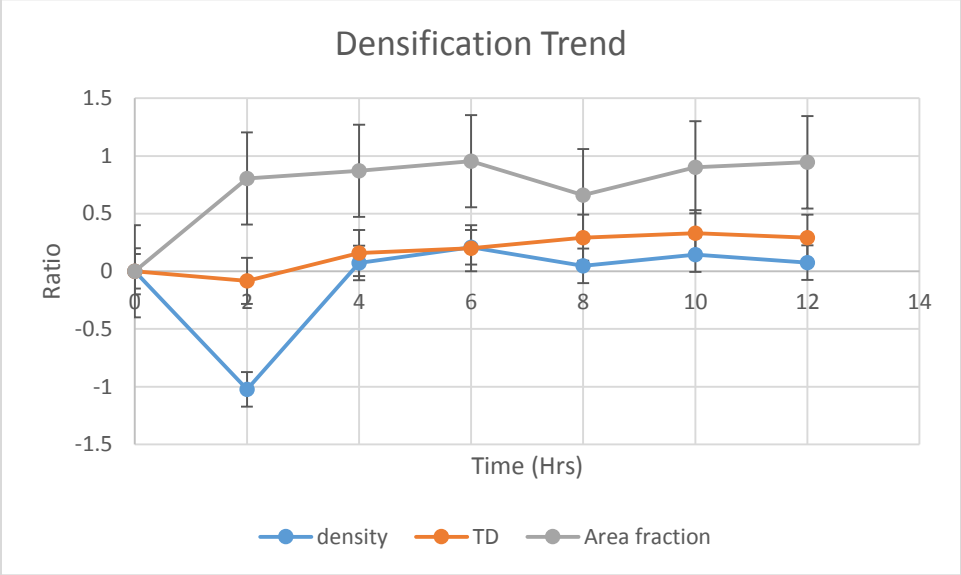

Figure 6-1: Observable densification trend

Porous U-10Zr pellets were produced with initial densities ranging from 61 to 88 %TD. The final sintered densities ranged from 69 to 87 %TD as measured dimensionally. However, area analysis of pores showed a marked increase of 92 to 98 %TD. The results observed are illustrated in Figure 6-1. The total densification, as observed, was divided by total possible densification (16.02 g/cc or 100 %TD subtracted by initial density or %TD) to normalize the curves. The dimensional results are likely skewed downward due to surface defects while the area analysis is likely skewed upward due to elimination of peripheral areas and sensitivity of the threshold.

Densification, while originally not evident due to competing mechanisms (stress

relaxation and diffusive alloying), was most notably observable above two hours sintering. Pores started sporadically mixed in the zirconium areas after pressing. From there, they were observed to diffuse towards the exterior of the uranium spheres and formed channels that reduced in width as sintering time increased. Meanwhile, zirconium rich rings formed around uranium spheres likely due to surface contamination of oxygen. These rings served as host to porosity as sintering progressed.

Estimates of diffusion were lower than observed trends as seen by EDS. The measurable diffusion zones where uranium diffused into zirconium were observed to be much larger. This was likely due to volumetric expansion due to differential diffusion rates and zirconium diffusion into the sphere increasing uranium diffusion rates outward.

Porous morphology began with coarsened, irregular concentrations in the zirconium pressed mass. As zirconium diffused, the pores migrated into uranium masses and enjoined the zirconium rings. The circularity was observed to provide a potential measure of sintering progress.

Additional data points could also help pin point the change in densification and morphology trends. Utilization of a more controlled atmosphere, with nitrogen monitoring, would improve impurity control. Another possible expansion in this study could be stress monitoring during sintering to actively monitor volume changes from relaxation and densification. Lastly, more data points at each time could help better understand these trends and qualify artifacts.

REFERENCES

[1] Michael R. Tonks, et al. “An object-oriented finite element framework for multiphysics phase field simulations.” *Computational Materials Science* 51.1 (2012): 20-29.

[2] "MOOSE Framework - Open Source Multiphysics." *Idaho National Lab,* [Online]. Available: https://mooseframework.inl.gov/ [Accessed 11 Feb. 2019].

[3] Bruce Berry and P. Millett. “Phase-field simulations of the impact of bimodal pore size distributions on solid-state densification.” *Journal of Nuclear Materials* 491 (2017): 48-54.

[4] Paul Millet et al. “Computational and Experimental Studies of Microstructure-Scale Porosity in Metallic Fuels for Improved Gas Swelling Behavior.” United States.

[5] Bruce Berry, *Numerical Simulation of Metallic Uranium Sintering,* MS Thesis University of Arkansas, 2017.

[6] A.P. Moore, et al. “Atomistic mechanisms of morphological evolution and segregation in U-Zr alloys.” *Acta Materialia* 115 (2016): 178-88.

[7] Yesinia Salazar and S. M. McDeavitt. *Title Pending.* MS Thesis. Texas A&M University. 2019. Thesis in progress.

[8] Chad Thompson. *A Rotating Electrode System for the Generation of Metal Alloy Microspheres.* MS Thesis. Texas A&M University, 2012.

[9] Daniel Galicki. *The Establishment, Characterization, and Use of a Rotating Electrode System for the Generation of Uranium Alloy Microspheres.* MS Thesis. Texas A&M University, 2014.

[10] “Uranium.” *AZO materials,* [Online]. Available: https://www.azom.com/properties.aspx?ArticleID=604 [Accessed 20 Feb. 2019].

[11] K. H. Eckelmeyer. “Residual Stresses in Uranium and Uranium Alloys.” (1987).

[12] B.W. Howlett and A. G. Knapton, 2nd UN International Conference on Peaceful Use of Atomic Energy, Geneva, Vol. 6, p.104, 1958.

[13] D. R. Mash and B. F. Disselhorst, Uranium-Zirconium Diffusion Studies, Oak Ridge, Tenn.: U.S. Atomic Energy Commission, Technical Information Service, 1955.

[14] S. A. Miller and P. R. Roberts, "ASM Handbook, Volume 7: Powder Metal Technologies and Applications," in *Rotating Electrode Process*, ASM International, 1998, pp. 97-101.

[15] C.R Clark, et al. "Production and Characterization of Atomized U-Mo Powder by the Rotating Electrode Process." *Argonne National Lab*, [Online]. Available: https://www.rertr.anl.gov/RERTR29/Abstracts/S15-2_Clarck.html [Accessed 21 Feb. 2019]

[16] O. D. Neikov, S. Naboychenko, V. G. Gopienko, I. B. Mourachova, I. V. Frishberg and D. V. Lotsko, Handbook of Non-Ferrous Metal Powders: Technologies and Applications, Elsevier, 2009.

[17] H. J. DeMita and S. A. Miller, "System and Method for Producing Fine Metallic and Ceramic Powders". United States of America Patent 5855642, 1999.

[18] C. R. Clark, J. F. Jue and B. R. Muntifering, "Production and Characterization of Atomized U-Mo Powder by the Rotating Electrode Process," in *INL?CON-07-13156*, Idaho Falls, 2007.

[19] C. R. Clark, J. F. Jue and B. R. Muntifering, "Production and Characterization of Atomized U-Mo Powder by the Rotating Electrode Process," in *INL.CON-07-13156*, Idaho Falls, 2007.

[20] A. Rollett, F. J. Humphreys, G. S. Rohrer *et al.*, *Recrystallization and Related Annealing Phenomena*: Elsevier Science, 2004.

[21] R.M. German, Sintering Theory and Practice, John-Wiley & Sons, Inc., New York, 1996.

[22] G. W. Helmreich and S.M. McDeavitt, *Uranium-Zirconium Alloys for Advanced Nuclear Fuel Applications*, College Station, TX: Texas A&M University, 2010.

[23] Z. Petru, Sinterung von polydispersen Glaspulvern, Silic. Ind. 36 (1971) 247.

[24] R.L. Coble, Effects of particle-size distribution in initial stage of sintering, J. Am. Ceram. Soc. 56 (9) (1973) 461.

[25] S.M. McDeavitt, *Hot Isostatic Pressing of U-10Zr Alloy Nuclear Fuel by Coupled Grain Boundary Diffusion and Power-Law Creep*, West Lafayette, IN: Purdue University, 1992.

[26] Agar Scientific, "MiniMet 1000," [Online]. Available: http://www.agarscientific.com/minimet-174-1000.html [Accessed 28 Feb. 2017].

[27] Leco, "VC50 Diamond Saw," [Online]. Available: http://www.leco.com/products/metallography-science/sectioning/vc50-diamond-saw [Accessed 28 Feb. 2017].

[28] J. Evans, personal communication, Aug. 5, 2016.

[29] J. Garcia et. al., *Nitrogen K-Shell Photoabsorption*. The Astrophysical Journal Supplement Series. (2009) 185. 477. 10.1088/0067-0049/185/2/477.